

1 Labrador Sea sub-surface density as a precursor of 2 multi-decadal variability in the North Atlantic: a multi-model 3 study.

4
5 Pablo Ortega^{1,2}, Jon I. Robson¹, Matthew Menary³, Rowan T. Sutton¹, Adam Blaker⁴, Agathe
6 Germe⁴, J el J.-M. Hirschi⁴, Bablu Sinha⁴, Leon Hermanson⁵ and Stephen Yeager⁶

7 ¹NCAS, University of Reading, Reading, UK

8 ²Barcelona Supercomputing Center, Barcelona, Spain

9 ³LOCEAN, Sorbonne Universit s

10 ⁴National Oceanography Centre, European Way, Southampton, SO14 3ZH, UK

11 ⁵Met Office Hadley Centre, Exeter, UK

12 ⁶National Center for Atmospheric Research, Boulder, USA

13 *Correspondence to:* Pablo Ortega (pablo.ortega@bsc.es)

14 **Abstract.** The Subpolar North Atlantic (SPNA) is a region with prominent decadal variability that has experienced
15 remarkable warming and cooling trends in the last few decades. These observed trends have been preceded by
16 slow-paced increases and decreases in the Labrador Sea density (LSD), which are thought to be a precursor of large
17 scale ocean circulation changes. This article analyses the inter-relationships between the LSD and the wider North
18 Atlantic across an ensemble of coupled climate model simulations. In particular, it analyses the link between
19 subsurface density and the deep boundary density, the Atlantic Meridional Overturning Circulation (AMOC), the
20 Subpolar Gyre (SPG) circulation, and the upper ocean temperature in the eastern SPNA.

21
22 All simulations exhibit considerable multidecadal variability in the LSD and the ocean circulation indices, which are
23 found to be interrelated. LSD is strongly linked with the strength of subpolar AMOC and gyre circulation, and is
24 also linked with the subtropical AMOC, although the strength of this relationship is model dependent and affected
25 by the inclusion of the Ekman component. The connectivity of LSD with the subtropics is found to be sensitive to
26 different model features, including: the mean density stratification in the Labrador Sea; the strength and depth of the
27 AMOC; and the depth at which the LSD propagates southward along the western boundary. Several of these
28 quantities can also be computed from observations, and comparison with these observation-based quantities suggests
29 that models representing a weaker link with the subtropical AMOC might be more realistic.

30 1. Introduction

31
32 The North Atlantic Ocean is a key component in Earth's climate through, for example, its role in redistributing heat
33 and in taking up excess heat and carbon from the atmosphere. It is also a region that has varied significantly in the
34 past. This is particularly true for the North Atlantic subpolar gyre, that has varied significantly on multi-decadal
35 timescales across a range of different variables (H kkinen and Rhines, 2004; Holliday et al., 2020; Reverdin, 2010;
36 Robson et al., 2018b). Basin-mean sea surface temperature (SST) over the North Atlantic has also been observed to
37 vary on multi-decadal timescales (Schlesinger and Ramankutty, 1994), and has been linked to a range of important
38 climate impacts, including hurricane numbers and rainfall in monsoon regions (Knight et al., 2006; Monerie et al.,
39 2019; Zhang and Delworth, 2006). The North Atlantic is also expected to change significantly in the future due to

40 the effects of climate change, and consequently produce substantial climate impacts on the surrounding regions
41 (Sutton and Hodson, 2005; Woollings et al., 2012). On decadal timescales, it is the interaction between natural
42 variability and externally forced changes that will shape how the Atlantic regions climate will evolve. Therefore, in
43 order to improve predictions of the North Atlantic, it is imperative that we improve our understanding of the
44 processes that control decadal timescale changes in this region.

45

46 It has generally been thought that changes in the ocean circulation, and particularly the Atlantic Meridional
47 Overturning Circulation (AMOC), have played a significant role in shaping the Atlantic Multidecadal Variability
48 (AMV; Knight et al. 2005). In particular, changes in the strength of the AMOC, and its related ocean heat transports
49 have been shown to control multi-decadal internal variability in a range of coupled climate models (Danabasoglu,
50 2008; Dong and Sutton, 2005; Jungclaus et al., 2005; Ortega et al., 2011, 2015). The proposed mechanisms to
51 explain the multi-decadal variability involve interplays between the North Atlantic Oscillation (NAO), North
52 Atlantic Deep Water (NADW) formation, the boundary currents, the Gulf Stream and gyre circulations, and the
53 horizontal density gradients (e.g. Joyce and Zhang, 2010; Polyakov et al., 2010; Ba et al., 2013; Nigam et al., 2018;
54 Zhang et al., 2019). Changes in AMOC and the wider ocean circulation have been indeed used to explain the
55 observed changes in the subpolar North Atlantic (SPNA) on decadal and longer timescales (Moat et al., 2019). In
56 particular, the SPNA underwent a rapid warming and salinification in the mid 1990s before a decadal timescale
57 cooling and freshening started in 2005, which is consistent with decadal-to-multidecadal variability of the AMOC
58 (Robson et al., 2012, 2013, 2016). The recent cooling has been linked to climate impacts over the continents,
59 including heat waves (Duchez et al., 2016), through an effect on the position on the jet stream (Josey et al., 2018). A
60 long term relative cooling of the SPNA since ~1850 has also been attributed to a centennial weakening of the
61 AMOC (Caesar et al., 2018; Rahmstorf et al., 2015), an AMOC reduction that most CMIP6 model projections
62 predict to continue in the future (Weijer et al., 2020). However, a lack of direct observations of the strength of the
63 AMOC or the ocean circulation more generally have hindered our ability to make a direct attribution of recent
64 changes.

65

66 In order to understand the aforementioned changes in the SPNA on multi-decadal timescales many authors have
67 turned to indirect measurements of the AMOC. One particular proxy of AMOC strength that has received some
68 focus recently are density anomalies at depth in the western SPNA or Labrador Sea region. In climate models,
69 density anomalies in the western SPNA are a key predictor of density anomalies further south on the western
70 boundary, and hence of the AMOC strength via thermal wind balance (Hodson and Sutton, 2012; Ortega et al.,
71 2017; Robson et al., 2014, 2016). Observations show considerable decadal variability in subsurface density
72 anomalies; density anomalies in the western SPNA or Labrador Sea between ~1000-2500 m increased significantly
73 and peaked in ~1995 and subsequently declined (Robson et al., 2016; Yashayaev and Loder, 2016). Therefore, these
74 density anomalies have been interpreted as indicating that the AMOC peaked circa mid-to-late 1990s, and then
75 declined, consistent with the warming and then cooling of the eastern SPNA (Hermanson et al., 2014; Ortega et al.,
76 2017; Robson et al., 2016). Time series of subsurface density anomalies in the western SPNA are also consistent
77 with other proxies of AMOC strength, including sea level based proxies (McCarthy et al., 2015; Sutton et al., 2018),
78 sediment based proxies (Thornalley et al., 2018), and upper ocean heat content fingerprints (Caesar et al., 2018;
79 Zhang, 2008). Furthermore, the decline in AMOC suggested by the above proxies is also consistent with the
80 observed AMOC decline at 26°N since 2004 (Smeed et al., 2018), and also with the changes in AMOC seen in
81 ocean data assimilation systems (Jackson et al., 2016, 2019). Therefore, there is confidence that large scale changes
82 in North Atlantic Ocean circulation have occurred over the past few decades, and that they have had a significant
83 impact on upper ocean heat content.

84

85 Although there is consistency across proxies of AMOC changes in the North Atlantic, there are considerable gaps in
86 our understanding and major uncertainties to overcome. For example, the development of the subsurface density
87 proxies has been investigated so far in just a few models (Ortega et al., 2017; Robson et al., 2014). However, there is

88 considerable spread across climate models in the simulations of AMOC mean state and variability (Reintges et al.,
89 2017; Zhang and Wang, 2013), and also in the latitudinal coherence of AMOC anomalies (Li et al., 2019; Roberts et
90 al., 2020; Hirschi et al., 2020), which might reflect different roles of deep density anomalies in the western SPNA on
91 the AMOC, as well as different interplays between the subpolar and subtropical gyre contributions (Zou et al.,
92 2020). Models also do not resolve realistically many key features of AMOC, most notably the overflows, and this
93 affects the subsurface stratification downstream and on the western boundary (Zhang et al., 2011). There also
94 remains significant uncertainty for other important processes. For example, it is not yet clear whether the recent
95 changes in the SPNA are an ocean response to buoyancy forcing, or whether mechanical wind forcing has shaped
96 the recent observed changes (Robson et al, 2016; Piecuch et al. 2017). Local surface fluxes are also likely to explain
97 a significant proportion of the recent cooling (Josey et al, 2018). Subsurface density anomalies are not just a proxy
98 for the AMOC, but more generally for buoyancy forced (or thermohaline) circulation changes, including gyre
99 changes (Ortega et al., 2017; Yeager, 2015). Finally, the AMOC variability is also thought to respond to local wind
100 forcing on a range of timescales, especially at lower latitudes (Polo et al., 2014; Zhao and Johns, 2014), which could
101 disrupt or “mask” the influence of subsurface density anomalies as they propagate further south.

102

103 There is also considerable uncertainty in how and where subsurface density anomalies are formed in the SPNA, and
104 how they are related to the AMOC. In observations and models, most water transformation associated with the
105 AMOC occurs within the SPNA, and particularly in the eastern SPNA (Desbruyères et al., 2019; Grist et al., 2014;
106 Langehaug et al., 2012). However, subsurface density anomalies in the western SPNA on decadal timescales have
107 often been linked with buoyancy forcing and changes in deep convection in the Labrador Sea or with changes in the
108 volume of Labrador Sea Water production (Yashayaev and Loder, 2016; Yeager and Danabasoglu, 2014). Many
109 studies have also reported that the basin-wide AMOC in ocean-only and coupled models is sensitive to heat flux or
110 buoyancy forcing in the Labrador Sea (Kim et al., 2020; Ortega et al., 2011, 2017; Xu et al., 2019; Yeager and
111 Danabasoglu, 2014). Indeed, idealised experiments have shown that persisting positive NAO phases can strengthen
112 the AMOC by fostering deep water formation via increased surface cooling in the Labrador Sea, thus inducing
113 changes in the zonal density gradient (Delworth and Zeng, 2016; Kim et al., 2020), and thermal wind responses.
114 However, the real link between deep convection, deep water formation, and density anomalies at depth in the
115 Labrador Sea is complex, and not fully understood (Katsman et al., 2018). Observations suggest that very little
116 water transformation and deep water formation actually occurs in the Labrador Sea (Pickart and Spall 2007; Lozier
117 et al., 2019). Indeed, recently it has been shown that the Labrador Sea (i.e. OSNAP-west) played very little role in
118 the interannual variability so far observed across the whole OSNAP line (Lozier et al., 2019), with the Irminger Sea
119 playing a more dominant role. The Irminger Sea is a region that in some models controls the AMOC and SPNA
120 variability, and that is especially sensitive to advective processes (Ba et al., 2013) and Arctic overflows (Fröb et al.,
121 2016). Moreover, ocean-only models appear to significantly overestimate the amount of deep water formed within
122 the Labrador Sea, with likely implications for coupled models (Li et al., 2019). These inconsistencies raise the
123 question of whether models are simulating the right relationships.

124

125 In this study we will address some of the above uncertainties by performing a multi-model analysis of the North
126 Atlantic in coupled climate models. We focus on the question of how robust is the relationship between subsurface
127 Labrador Sea density anomalies and the basin-wide Atlantic Ocean circulation on decadal timescales. We also assess
128 the question of whether Labrador Sea density can robustly induce density changes over the western continental slope
129 and generate a geostrophic response in the meridional circulation (Bingham and Hughes, 2009; Roussenov et al.,
130 2008). Shedding new light on these links is important for, among other reasons, determining to what extent the
131 RAPID measurements represent the variability of the basin-wide AMOC cell, as well as to identify the models that
132 can produce more reliable predictions and projections of the SPNA. For this, we will assess specifically the
133 connection between subsurface density and AMOC at high and low latitudes via the western boundary. Furthermore,
134 we will determine whether models consistently support an impact of AMOC changes on the SPNA upper ocean
135 temperatures, and if not, investigate why. Our primary aim is to provide, for the first time in a multi-model context,

136 a broad characterization of these relationships using consistent analysis frameworks and tools, and to document the
137 uncertainty. The reasons for the uncertainty in the relationships will also be explored, establishing links with key
138 model climatological properties that could eventually be exploited as emergent constraints. We intentionally do not
139 explore in detail how subsurface density anomalies are formed in these models, and leave this for further study.

140

141 The paper is organised as follows. Section 2 describes the experiments and methods. Labrador Sea density, and its
142 link with the ocean circulation and the wider North Atlantic are explored across the multi-model ensemble in
143 Section 3. The characteristics of the intermodel spread in the previous relationships are explored in Section 4, and
144 Section 5 presents the main conclusions of this study and discusses its implications.

145

146

147 **2. Experiments and methods**

148

149 Here we provide an overview and brief description of the models used in this study and provide some statistical
150 considerations for the intermodel comparison.

151

152 **2.1. Experiment selection**

153

154 For the multi-model analysis, we use the preindustrial control simulations (picontrol) from the fifth phase of the
155 Coupled Model Intercomparison Project (CMIP5; Taylor et al. 2012), in which forcing values of GHGs, aerosols,
156 ozone and solar irradiance are fixed to 1850 levels. We chose to use control over historical simulations to focus
157 exclusively on internal variability and benefit from the more robust statistics that the long preindustrial experiments
158 provide. Furthermore, we avoid the forced trends present in the historical experiments, which can lead to
159 correlations that are difficult to interpret objectively (Tandon and Kushner, 2015). From the CMIP5 ensemble, we
160 only use those models in which 3D fields of ocean temperature and salinity, as well as the streamfunctions of
161 meridional overturning circulation and/or the barotropic circulation, were available. Twenty different models meet
162 this condition. Their main characteristics and number of simulation years have been summarized in Table 1. Most of
163 the models have a nominal horizontal resolution in the ocean close to 1° , and, therefore, cannot resolve the effects of
164 eddies. Menary et al. (2015) has shown for these same model simulations that the effective horizontal resolution can
165 be higher over the Labrador Sea, due to the non-regular grids. Effective resolutions over the Labrador Sea area range
166 from 0.21° in the GC2 model to 1.1° in GISS-E2-R/GISS-E2-R-CC/CanESM2, with these differences determining
167 to a large extent the mean state model biases and the dominant drivers (i.e. salinity or temperature) of the Labrador
168 Sea density changes.

169

170 Complementing these simulations, we also consider two control experiments with eddy-permitting resolutions.
171 Specifically, we use a present day control simulation (i.e. with fixed radiative forcing levels from year 1990) of the
172 HiGEM model, with nominal horizontal resolution in the ocean of $1/3^\circ$, and of 0.83° latitude \times 1.25° longitude in
173 the atmosphere (Shaffrey et al., 2009), and a pre-industrial control of HadGEM3-GC2 (hereafter, GC2; Ortega et al.
174 2017) with a nominal resolution in the ocean of $1/4^\circ$ (ORCA025) and N216 in the atmosphere (i.e. approximately 60
175 km in the mid-latitudes). The GC2 simulation is the same one employed for the previous analyses of Labrador Sea
176 variability in Robson et al. (2016) and Ortega et al. (2017). Note that we will assume that the present day control in
177 HiGEM can be compared with the other preindustrial simulations due to the large uncertainty these later show in
178 their climatological biases, and so, for the sake of simplicity, we will only refer to preindustrial control experiments
179 from now on. [Figure 1](#) demonstrates that this assumption is reasonable, since the mean Labrador Sea stratification in
180 HiGEM is very similar to that in the other models.

181

182 As an observationally-constrained reference, this study also includes the assimilation run from DePreSys3, a decadal
183 prediction system from the MetOffice based on GC2 (Dunstone et al., 2016). In the ocean, the assimilation is

184 performed through a strong nudging (ten-day relaxation timescale) towards the full fields of a three-dimensional
 185 objective temperature and salinity analysis (Smith and Murphy, 2007). Since it covers a comparatively shorter
 186 period (1960-2013), and therefore different timescales than the control experiments, its comparison with the other
 187 simulations will be done with caution, in particular regarding the indices of the large-scale Atlantic circulation, for
 188 which other assimilation products show important discrepancies (Karspeck et al., 2015), thus highlighting
 189 significant uncertainty. For evaluation purposes, we also use EN4.2.1 (Good et al., 2013), an objective analysis of
 190 monthly temperature and salinity 3D observations developed at the MetOffice.

191
 192
 193
 194

Table 1: List of the models used for this study, their characteristics and those of their picontrol simulations. For further details on the CMIP5 model configurations and components please refer to Table 9.A.1 in Flato et al. (2013) and references therein.

Model ID	Lon x Lat ocean resolution (number of vertical levels)	Length	Key variables available
HadGEM3-GC2	1/4° x 1/4° (75 levels)	311 years	AMOC, SPGSI, LSD, NOHT
HiGEM	1/3° x 1/3° (40 levels)	341 years	AMOC, SPGSI, LSD, NOHT
ACCESS1-0	1° x 1° enhanced near Equator and high latitudes (50 levels)	500 years	SPGSI, LSD, NOHT
ACCESS1-3	1° x 1° enhanced near Equator and high latitudes (50 levels)	500 years	SPGSI, LSD, NOHT
CCSM4	1.125° x 0.27–0.64° (60 levels)	1051 years	AMOC, SPGSI, LSD
CESM1-BGC	1.125° x 0.27–0.64° (60 levels)	500 years	AMOC, LSD
CESM1-CAM5	1.125° x 0.27–0.64° (60 levels)	319 years	AMOC, LSD
CESM1-FASTCHEM	1.125° x 0.27–0.64° (60 levels)	222 years	AMOC, LSD
CESM1-WACCM	1.125° x 0.27–0.64° (60 levels)	200 years	AMOC, LSD
CNRM-CM5	0.7° x 0.7° (42 levels)	850 years	AMOC, SPGSI, LSD
CanESM2	1.4° x 0.93° (40 levels)	996 years	AMOC, SPGSI, LSD
FGOALS-g2	1° x 1° with 0.5° meridional in the tropical region (30 levels)	700 years	AMOC, LSD
FGOALS-s2	1° x 1° with 0.5° meridional in the tropical region (30 levels)	501 years	SPGSI, LSD, NOHT
GFDL-ESM2G	1° x 0.85° (63 levels)	500 years	SPGSI, LSD
GISS-E2-R	1.25° x 1° (32 levels)	550 years	AMOC, LSD
GISS-E2-R-CC	1.25° x 1° (32 levels)	251 years	AMOC, LSD
MPI-ESM-LR	1.5° x 1.5° (40 levels)	1000 years	AMOC, SPGSI, LSD

MPI-ESM-MR	0.4° x 0.4° (40 levels)	1000 years	AMOC, SPGSI, LSD
MPI-ESM-P	1.5° x 1.5° (40 levels)	1156 years	AMOC, SPGSI, LSD
MRI-CGCM3	1° x 0.5° (51 levels)	500 years	AMOC, LSD, NOHT
NorESM1-M	1.125° x 1.125° (53 levels)	501 years	AMOC, SPGSI, LSD, NOHT
NorESM1-ME	1.125° x 1.125° (53 levels)	252 years	AMOC, SPGSI, LSD, NOHT

195

196

2.2. Methodological considerations

197 Density values are computed from 3D salinity and potential temperature fields, using the International Equation of
 198 State of seawater (EOS-80), and are referred to the level of 2000 dbar (σ_2), to give a stronger emphasis to the deep
 199 water properties.

200 Statistical significance of correlation coefficients is assessed following a two-tailed Student's t-test that takes into
 201 account the series' autocorrelation to correct the sample size, reducing the degrees of freedom of a series to its
 202 effective value (Bretherton et al., 1999).

203 Because our goal is to provide further insight into the suggested relationships established from observed trends in
 204 the North Atlantic (e.g., Robson et al., 2016), all statistical analyses in this study exploring the relationships between
 205 variables and associated lags are based on 10-year running trends. This is analogous to the calculation of a typical
 206 10-year running mean, but computing over each 10 year period a linear trend instead and keeping the slope value.
 207 Note also that our main results remain similar if decadal running means are applied instead (not shown), as both are
 208 alternative approaches to concentrate on the low-frequency variability. Running trends have also the particular
 209 advantage of not being sensitive to long-term drifts, which are still present (and can be important for some
 210 simulations and variables) when running means are computed. To illustrate how decadal running trends represent
 211 low-frequency variability, and how they compare with the decadal running means, both have been included in
 212 [Figure 2b](#) (solid thick lines vs dashed thin lines) for an index of Labrador Sea density.

213

214 3. Labrador Sea density as an index of multi-decadal North Atlantic variability

215

216 This section explores the potential of Labrador Sea density as a proxy of the ocean circulation changes in the North
 217 Atlantic. As in our previous studies (Ortega et al., 2017; Robson et al., 2016), the indices that we will herein define
 218 represent waters within the Labrador Sea and not those that are necessarily formed in the region (e.g. Labrador Sea
 219 Water). Since Labrador Sea variability is affected by different processes (e.g. vertical mixing, Arctic-Atlantic
 220 overflows, sea ice interactions) that can be represented differently in the models, both in time and space, we
 221 characterize its variability over a relatively broad box (60°W-35°W; 50°N-65°N, blue box [Figure 1a](#)) that also
 222 includes part of the Irminger Sea region. Note that over this large area EN4.2.1, shows the weakest density
 223 stratification in the North Atlantic (characterised in [Figure 1a](#) as the density difference between 1000m and the
 224 surface).

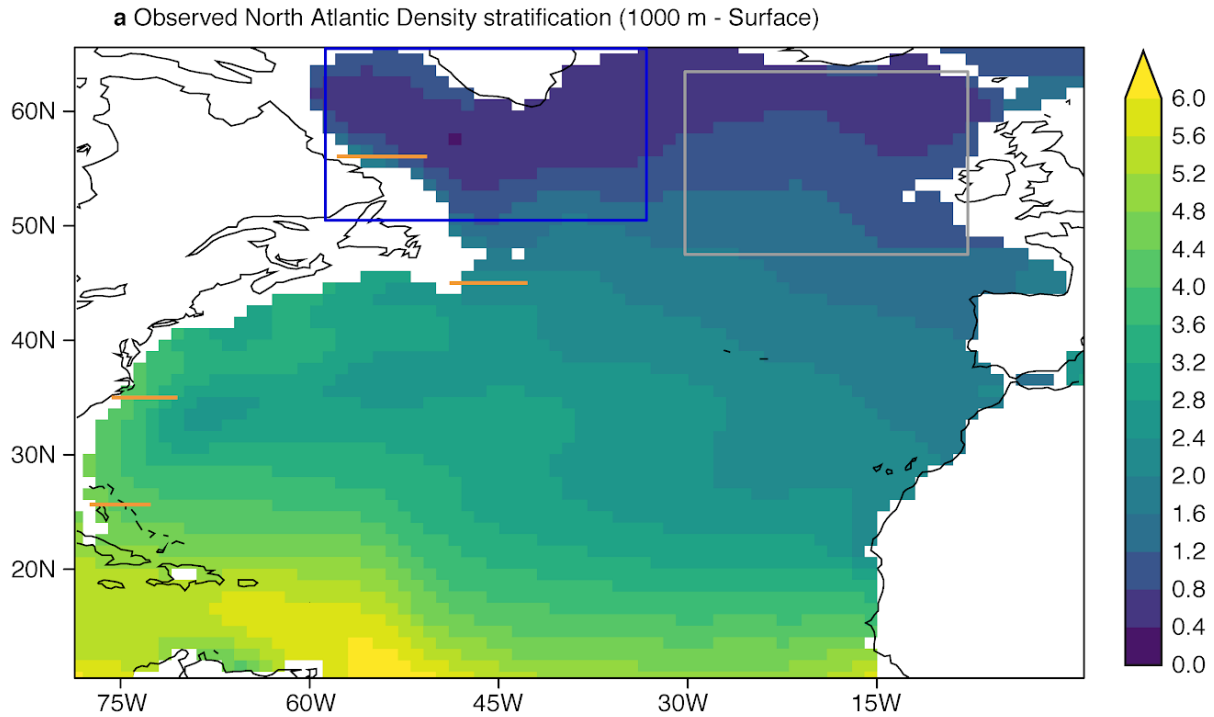
225 3.1. Labrador Sea density across models

226 A first indicator of potential model discrepancies is Labrador Sea stratification, which can lead to differences in the
 227 representation of deep ocean convection (i.e. weaker density stratifications will facilitate the mixing, fostering
 228 convection activity, and vice versa for stronger density stratifications). [Figure 1b-d](#) illustrates the inter-model

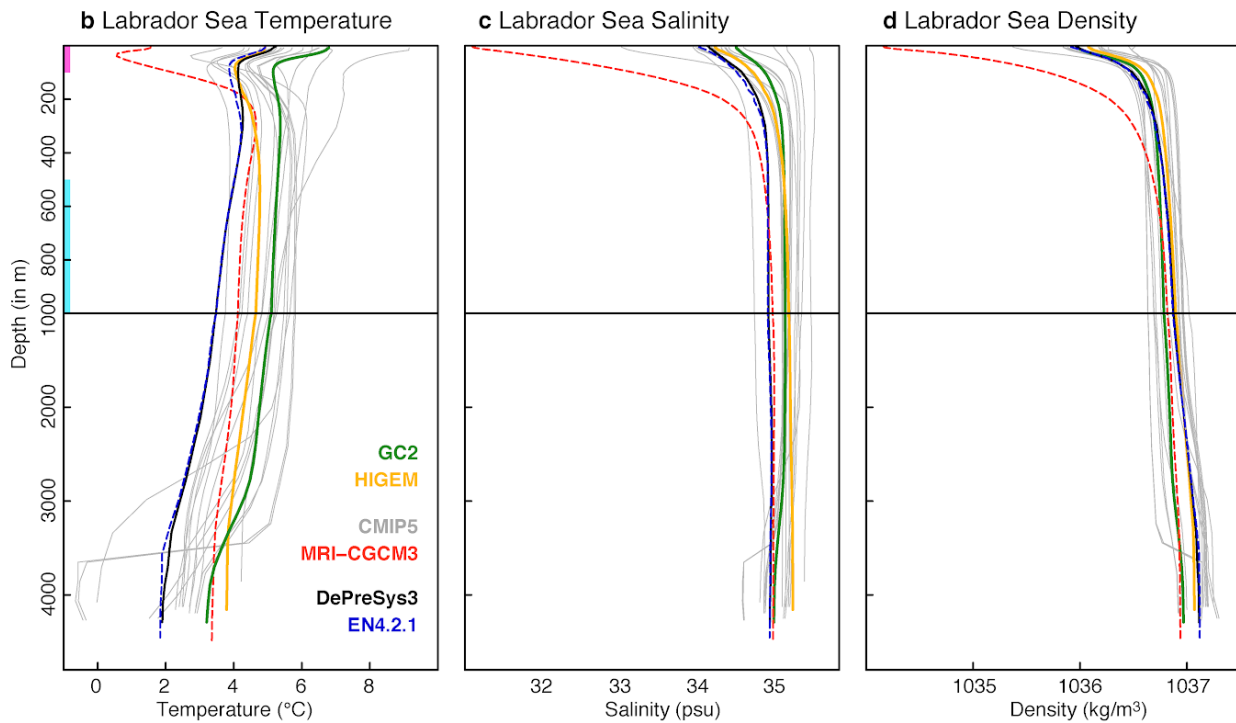
229 differences with the vertical profile of the spatially averaged Labrador Sea temperature, salinity and density. The
230 largest discrepancies are seen for temperature. Most models present their warmest waters at the surface, and
231 temperatures decrease sharply to minimum values around 100 m and increase again at deeper levels, reaching
232 uniform conditions after approx 300 m. However, the location and magnitude of this temperature minimum and the
233 two maxima are highly variable. It is important to note that the profile for one of the models, MRI-CGCM3, is
234 noticeably different to the others, with a subsurface minimum more than 2 degrees colder than for any of the other
235 models. In terms of salinity, the general profile is more coherent across models, with minimum salinity at the surface
236 that progressively increases with depth and attains uniform values after 500 m. Density stratification seems to be
237 determined by salinity, as their two vertical profiles show similar features. This similarity includes exceptionally
238 strong density and salinity stratification in MRI-CGCM3 as compared with the other models. This stratification is so
239 strong that it precludes the occurrence of deep convection (not shown). Because of this, MRI-CGCM3 is an outlier
240 for many of the metrics used in the paper, and has been excluded for the subsequent analyses to facilitate the
241 interpretation of our results. We also note that the profiles for the two eddy-permitting models (green and orange
242 lines in [Figure 1b,d](#)) lie within the spread of the CMIP5 models, indicating that resolution (at least to
243 eddy-permitting spatial scales) does not drastically change stratification in the region. The DePreSys3 assimilation
244 run closely matches the stratification in EN4.2.1, which supports DePreSys assimilation run as a reasonable
245 observation-constrained reference for the models. The comparison of both observation-based datasets with the rest
246 of simulations suggests that, in the subsurface, all models are too warm and most of them are too salty, two biases
247 that have a competing effect on the mean subsurface density. Because of these canceling effects, several models
248 show a comparatively better representation of the subsurface densities when compared to EN4.2.1 and DePreSys3.
249 This compensation of model shortcomings for temperature and salinity is clearly illustrated in HiGEM, which shows
250 a remarkable agreement with EN4.2.1 below 500 m.

251 To represent the characteristic interannual variability of Labrador Sea densities (hereafter referred to as LSD for
252 consistency with previous work), we perform an Empirical Orthogonal Function (EOF; Storch and Zwiers, 1999)
253 analysis and extract the leading mode for the spatially averaged annual means of LSD ([Figure 2a](#)), as in Ortega et al.
254 (2017). For all simulations the first EOF of LSD exhibits a vertical structure where density values are largest at or
255 near the surface and gradually decrease with depth. Thus, this first EOF typically reflects situations in which the
256 density stratification, as described by the climatological vertical profile in [Figure 1d](#), is weakened or strengthened,
257 which happens when the corresponding principal component takes positive and negative values, respectively. Some
258 inter-model discrepancies are evident, in particular regarding the depths where the maximum density values are
259 found, which can happen between the surface and 500 m. Despite these differences, the dominant timescales of LSD
260 variability seem to coincide between models. For example, [Figure 2b](#) illustrates the first principal component of
261 LSD (PC1-LSD) for GC2 and HiGEM, showing in both cases clear multidecadal variability. Furthermore, [Figure 2c](#)
262 shows the Fourier spectrum analysis of the annual PC1-LSD values, and most models show enhanced PC1-LSD
263 variability for periodicities between 5 and 30 years.

264 In addition to the PC1-LSD index we consider a deep LSD index as introduced in Robson et al (2016). The deep
265 LSD index is defined as the 1000-2500 m vertical mean of the spatially averaged density over the same region as
266 PC1-LSD. We now compare how both indices represent the low-frequency changes in LSD, described in this paper
267 as decadal running trends. A lead-lag correlation between the decadal trends in both PC1-LSD and deep LSD
268 indices shows that they are strongly correlated in all models. However, some differences emerge when considering
269 the lag of maximum correlation ([Figure 2d](#)). This comparison might indicate, once again, that decadal variability of
270 subsurface density is concentrated at different depths in different models. It is also possible that both indices are
271 sensitive to changes in deep water formation in different locations (e.g. Irminger or GIN Seas), which could, hence,
272 affect the depth and maximum lag of the correlations. Nevertheless, we adopt PC1-LSD for the rest of the analyses,
273 as it has the advantage of adjusting in each model to the depths in which density variability is more prominent.

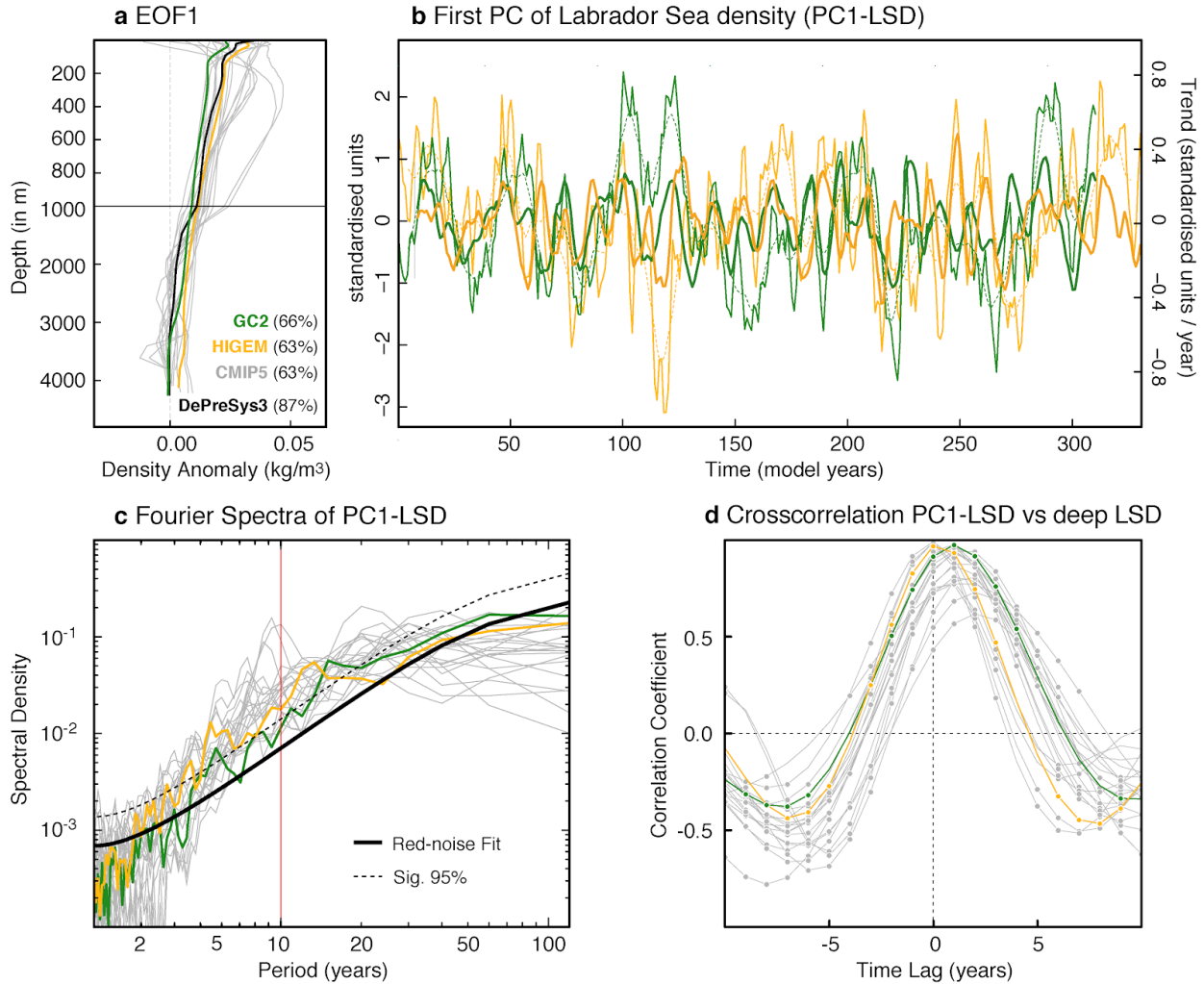


274



275 **Figure 1:** **a** Climatological density (computed as σ_2 at all depth levels) difference between the subsurface (1000m)
 276 and surface in the North Atlantic in the observational dataset EN4.2.1 (Good et al., 2013). The reference period to
 277 compute the climatology is 1960-2013. The grey box (32°W-10°W and 47°N-63°N) encloses the region where the
 278 ESPNA-T700 index in [Figure 4d](#) is computed. **b-d** Climatological mean of the spatially averaged Labrador Sea
 279 (60–35°W, 50–65°N, blue box in panel *a*) temperature, salinity and density as a function of depth in the simulation
 280 ensemble, the DePreSys3 assimilation run and EN4.2.1. The magenta (cyan) bars in the vertical axis correspond to

281 the depths that have been used to define the vertical stratification Labrador Sea indices. The horizontal orange lines
 282 by the North American coast represent the location of the latitudinal cross-sections in [Figure 10](#) and [Figure 11](#). For
 283 each model and dataset the climatology is computed for its whole length exceptv for EN4.2.1, that is computed for
 284 the overlap period with the DePreSys3 assimilation run.



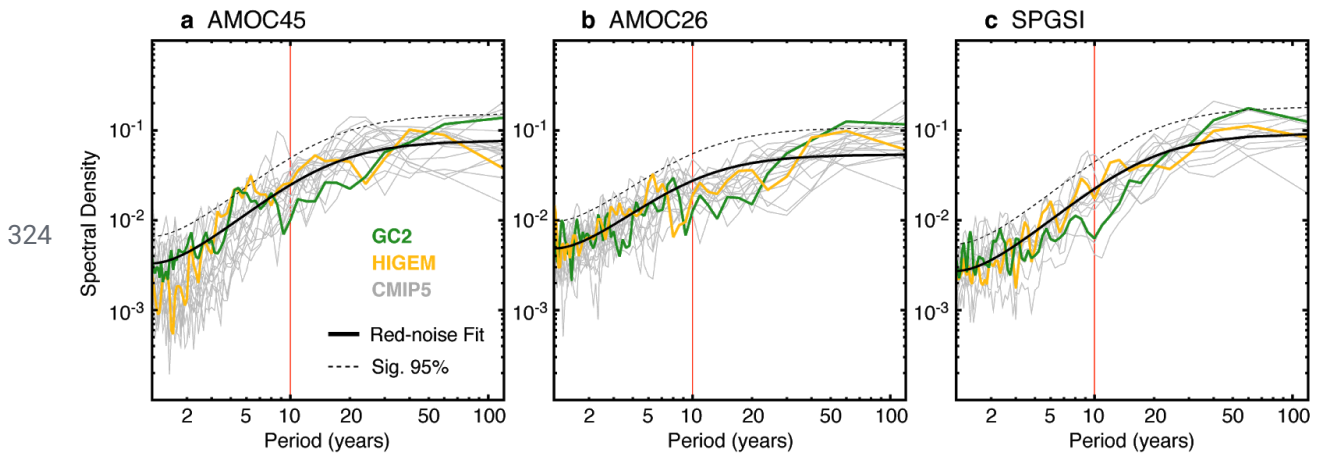
285

286 **Figure 2:** **a** First empirical orthogonal function (EOF) as a function of depth of the spatially averaged LSD in all the
 287 preindustrial experiments and in the DePreSys3 assimilation run. The percentage of variance explained by this mode
 288 in each model is included in brackets in the legend (for the CMIP5 runs, this represents the mean value across the
 289 ensemble). Because the sign of an EOF is arbitrary, it has been adjusted for all models (together with the sign of the
 290 respective principal component) so that both represent an increase in density stratification. **b** Associated principal
 291 component of the spatially averaged LSD (PC1-LSD) in the two high-resolution experiments. The thin solid lines
 292 represent the raw yearly-resolved PC1-LSD timeseries, the thin dashed lines their respective 10 year running means,
 293 and the thick (and slightly darker) lines their associated 10-year running trends (centered around the last year of the
 294 decade over which the trend is computed). **c** Normalized Fourier spectra of the PC1-LSD index in each of the
 295 preindustrial simulations. The black thick line represents a red noise process with the same first autoregressive
 296 (AR1) coefficient as PC1-LSD in GC2, and the dashed line sets the 95% confidence interval of this red-noise
 297 process. No major differences are found when using HiGEM's AR1 coefficient instead. The red vertical line
 298 highlights the 10 year periodicity to separate the interannual from the decadal to multi-decadal timescales. **d**

299 Lead-lag correlations between the decadal trends in PC1-LSD, and those in the deep LSD index from Robson et al.
 300 (2016), defined as the 1,000–2,500 m average density in the box 60–35°W, 50–65°N. Positive lags indicate that
 301 PC1-LSD leads the changes in deep LSD. Full dots denote correlation values exceeding a 95% confidence level
 302 based on a student’s t-test that takes into account the series autocorrelation.

303 3.2. Labrador Sea density linkages with the ocean circulation

304 The link between PC1-LSD and other ocean circulation indices in the North Atlantic is now examined. Three
 305 indices are considered: the AMOC at two different latitudes, 26°N (i.e. the same latitude as the RAPID array) and
 306 45°N to capture the typical variability of the subpolar AMOC, and an index of the subpolar gyre strength. The
 307 AMOC indices are computed as the maximum of the North Atlantic overturning circulation at any depth.
 308 Furthermore, the Ekman component is removed to focus on the slow wind-forced and the thermohaline-driven (i.e.
 309 the only one that can be influenced by the PC1-LSD directly) AMOC changes. To compute the Ekman component,
 310 we vertically integrate the Ekman velocities (after introducing a depth-uniform return flow to ensure no net
 311 meridional mass transport), following Eq. 6 in Baehr et al. (2004) with a fixed Ekman layer depth of 50 meters. This
 312 Ekman component is then removed at each depth level, prior to the calculation of the AMOC indices. The subpolar
 313 gyre strength is computed as an average of the North Atlantic barotropic streamfunction in the Labrador Sea region
 314 (60–35°W, 50–65°N), where the gyre strength is usually maximum. Since the SPG circulation is cyclonic and,
 315 therefore, associated with negative barotropic streamfunction values, the subpolar gyre strength index (SPGSI) is
 316 multiplied by -1 so that an intensification of the gyre corresponds to a positive value of the index. The Fourier
 317 spectra of the raw ocean circulation indices (Figure 3) show that, similar to the PC1-LSD, all three indices have
 318 strong multidecadal variability, with the largest differences with respect to PC1-LSD emerging for the timescales
 319 between 10 and 30 years, in which the spectral power is comparatively weaker, in particular for the AMOC26 index,
 320 and at 50 and longer timescales, in which the ocean circulation indices appear to have enhanced variability with
 321 respect to PC1-LSD. Similar spectra, but with enhanced variance at short timescales and reduced variance at the
 322 longest timescales are obtained for the AMOC indices when the Ekman component is kept (Supplementary Figure
 323 1), which suggests that the low-frequency processes dominate the total AMOC variability.



325 **Figure 3: a-c** Fourier spectra in the piconontrol ensemble for the indices AMOC45, AMOC26 and SPGSI. Red-noise
 326 spectra corresponding to a 1st order autoregressive process fit to GC2 indices are provided as reference.

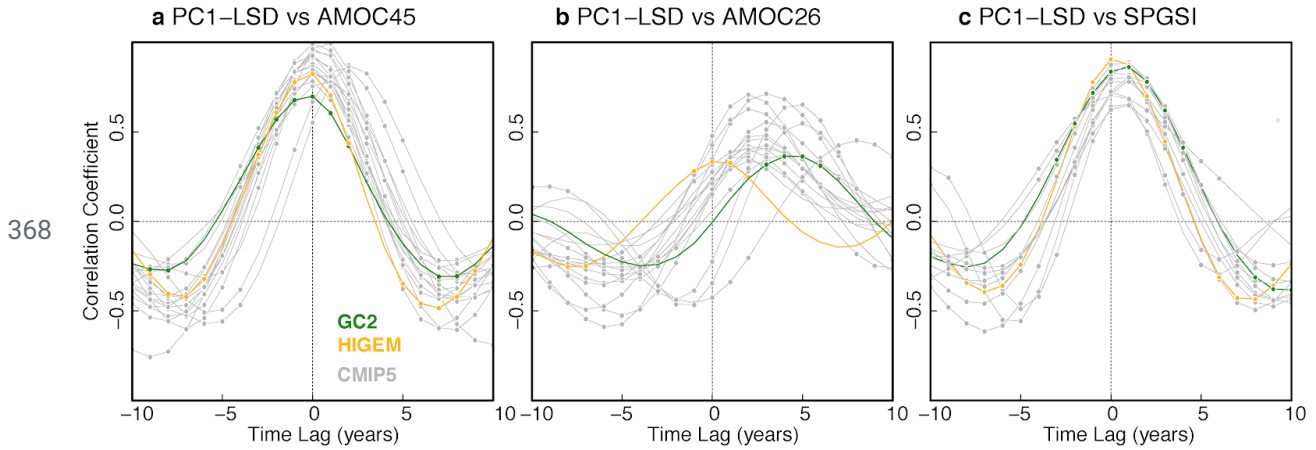
327 Figure 4a shows that decadal trends in PC1-LSD are associated with trends in the AMOC at 45°N (AMOC45).
 328 Nevertheless, there is some inter-model spread regarding the lag of maximum correlation, which ranges between 0
 329 and 2 years (with PC1-LSD leading), although both variables are in phase for the majority of models. The AMOC at
 330 26°N (AMOC26) is also positively related to PC1-LSD, with PC1-LSD leading AMOC26 by three years on average

331 (Figure 4b). However, the average correlation between PC1-LSD and AMOC26 is weaker, and the spread in the
332 magnitude and lag of the maximum correlation is larger than for AMOC45. Therefore, it appears that the link with
333 the subtropics is weaker than for 45°N and that AMOC coherence between subpolar latitudes and the subtropics in
334 coupled models is model dependent. This weaker link of PC1-LSD with the subtropical AMOC is not surprising, as
335 the LSD anomalies need to propagate a longer distance along the western boundary, allowing for model differences
336 in the representation of ocean currents and gyres to impact the timing and magnitude of the maximum correlations.
337 The reasons for the spread in the relationship between PC1-LSD and AMOC26 are explored in Section 4. A strong
338 relationship is also found between PC1-LSD trends and those in SPGSI (Figure 4c), of similar order than for
339 AMOC45. Thus, overall, PC1-LSD is a good proxy for the large-scale ocean circulation in the Subpolar North
340 Atlantic, and can also be a precursor for a fraction of the AMOC variability in the subtropical Atlantic.

341 PC1-LSD is also a good precursor of the full AMOC variability (i.e. including the Ekman transport), although the
342 wind-induced fluctuations associated with the Ekman component can introduce differences in the lags of the
343 maximum AMOC vs PC1-LSD correlations (Supplementary Figure 2). This different lag can be explained by the
344 fact that when the Ekman component is included, the AMOC contains a signal that is instantaneously driven by
345 basin-scale surface wind anomalies (such as the NAO) that are, ultimately, also linked to the heat loss in the
346 subpolar North Atlantic, which induces a delayed influence on the PC1-LSD (Ortega et al. 2017). Hence, including
347 Ekman can lead to counterintuitive relationships in some models, in which the AMOC appears to lead the PC1-LSD
348 changes. Also, in the particular case of GC2, the interference of the two signals (i.e. the subtropical Ekman and the
349 delayed PC1-LSD) turns the correlations in Supplementary Figure 2d insignificant, masking out the real influence of
350 PC1-LSD on the subtropics. For those reasons, and to ease the interpretation of the lagged-relationships, the rest of
351 the analysis is exclusively focused on the AMOC indices without ekman.

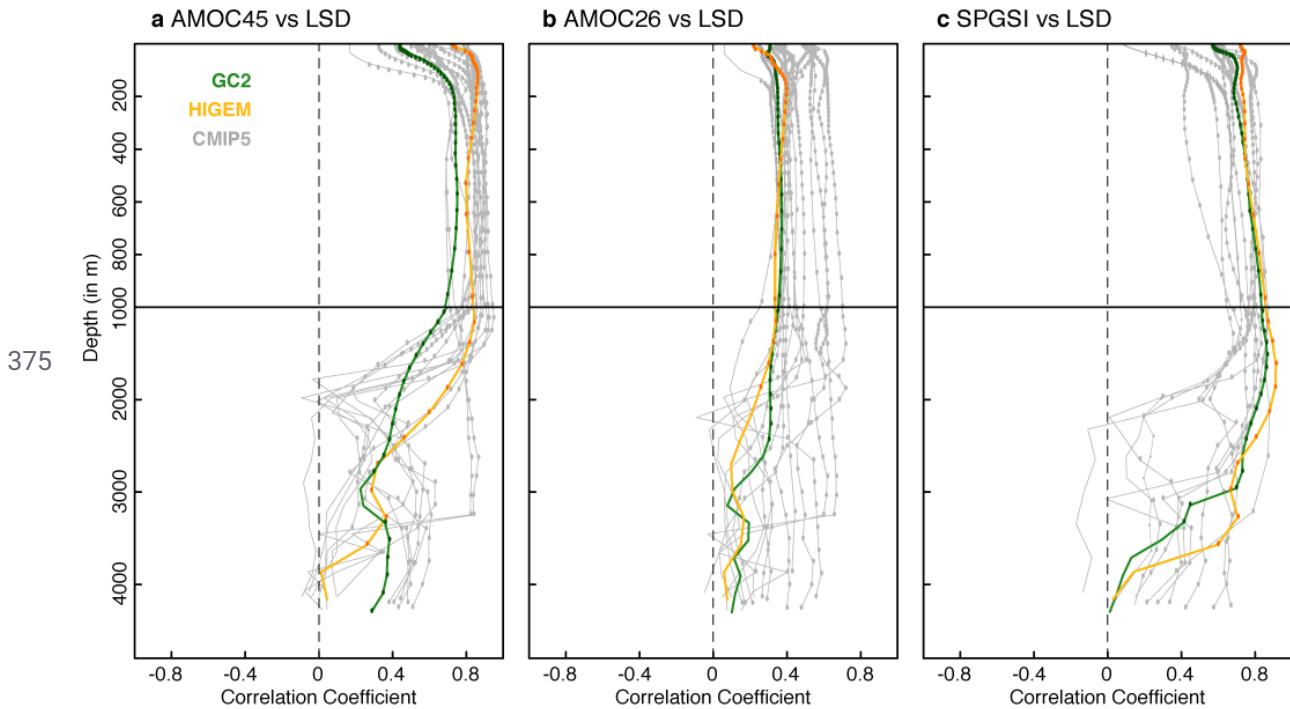
352 The role of PC1-LSD as a precursor of the AMOC is further supported by a parallel analysis in Figure 5, looking at
353 the maximum correlation between the decadal AMOC trends and those in Labrador Sea density as a function of
354 depth, when the latter leads the AMOC by up to 10 years. Figure 5 reveals that the strongest link between the
355 Labrador Sea densities and the AMOC, both at 45 and 26°N, occurs in its first 1000 m, the same levels where the
356 first EOF of LSD show the maximum loadings (Figure 2a), which confirms the appropriateness of using PC1-LSD
357 to represent the ocean circulation. The same analysis also supports a strong link between SPGSI and LSD, although
358 in that case the largest correlations usually happen at deeper levels (between 1000 and 2000 m). Note also that the
359 main conclusions drawn from PC1-LSD are also valid for the deep LSD index: however, the inter-model differences
360 are larger in the cross-correlations with the AMOC indices (Supplementary Figure 3). This difference could reflect
361 that the deep LSD index is more sensitive to other influences, like the Arctic overflows (Ortega et al., 2017), which
362 can be very differently represented across models. Overall, the PC1-LSD index seems to be a better choice to
363 describe multi-decadal North Atlantic variability in multi-model comparisons, as it selects the key depths for each
364 model. However, PC1-LSD is mostly focused on near surface levels and, therefore, likely represents mostly
365 Labrador Sea forced variability. Other indices describing densities at deeper levels might be preferable to compare
366 Labrador Sea Waters of different origins across models, and to evaluate their realism against observations.

367



369 **Figure 4:** a Lead-lag correlations across the picontrol ensemble between the PC1-LSD index and the maximum
 370 AMOC streamfunction at 45°N after the Ekman transport is removed (AMOC45). Correlations are based on 10-year
 371 running trends. Significance is assessed as in [Figure 2d](#) and indicated with a circle. For positive lags, PC1-LSD
 372 leads. **b-c** The same as in *a* but between PC1-LSD and the maximum AMOC streamfunction at 26°N after the
 373 Ekman transport is removed (AMOC26) and the subpolar gyre strength index (SPGSI).

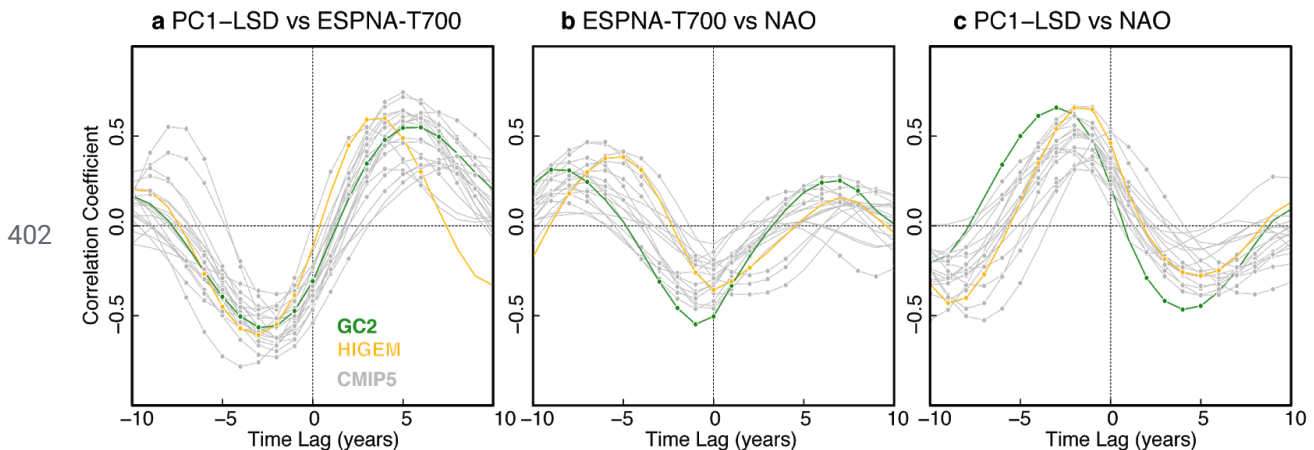
374



376 **Figure 5:** a Maximum correlation (for any lag between 0 and 10 years) between the AMOC45 index (after the
 377 Ekman transport is removed) and Labrador Sea Densities as a function of depth for all the simulations. Colored dots
 378 indicate correlations that are significant at the 95% confidence level. **b-c** The same as in *a* but between the
 379 AMOC26 index and LSD, and between the SPGSI and LSD, respectively.

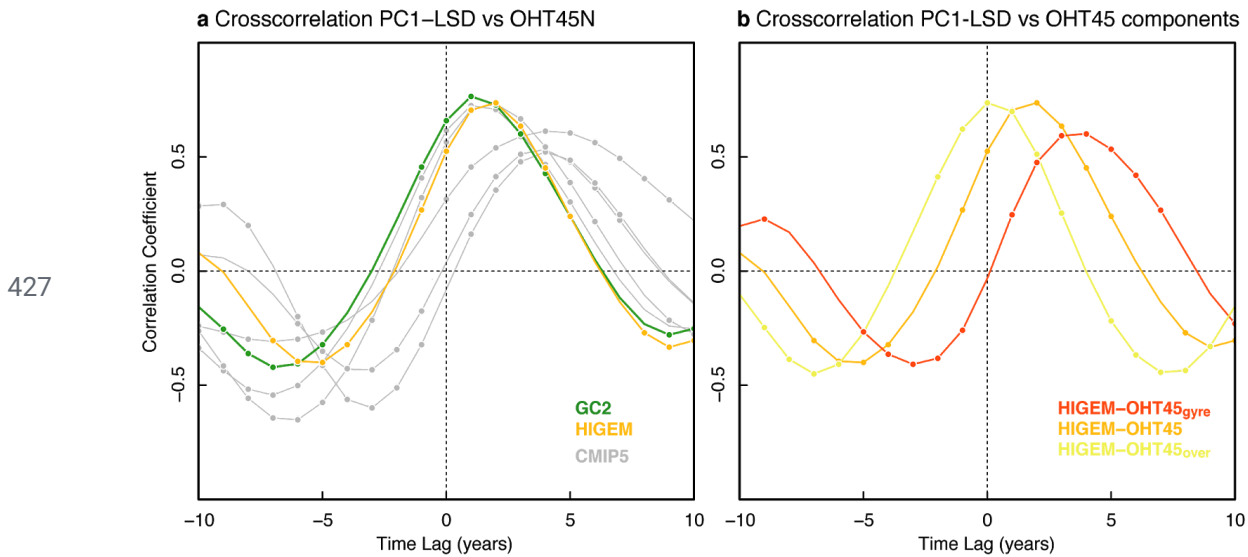
3.3. Labrador Sea density linkages with the wider North Atlantic

382 Previous studies based on the GC2 picontrol simulation have suggested LSD to be also a potential predictor of
 383 wide-spread cooling events in the eastern SPNA, like the observed cooling over 2005 to 2014 (Robson et al. 2016;
 384 Ortega et al. 2017). We thereby continue our exploration of the PC1-LSD index by investigating its link with the
 385 eastern SPNA in the multi-model ensemble. To explore this link we introduce a new index that represents the mean
 386 potential temperature in the eastern SPNA region (32°W - 10°W , 47°N - 63°N) averaged over the top 700 m of the
 387 ocean (ESPNA-T700). Lead-lag correlations between the decadal trends in PC1-LSD and this index (Figure 6a)
 388 show that there is a coherent relationship between both variables across models, with PC1-LSD increases
 389 (decreases) being consistently followed by ESPNA-T700 warmings (coolings). Nevertheless, there are inter-model
 390 differences concerning the magnitude and lag of the strongest positive correlations, revealing important uncertainty
 391 in the relationship. The spread in the PC1-LSD vs ESPNA-T700 relationship is thus reminiscent of the spread found
 392 between PC1-LSD and AMOC26, which suggests that they might be related. We also note significant negative
 393 correlations when ESPNA-T700 leads PC1-LSD by 2-4 years that might be explained by the opposed (and nearly
 394 concomitant) impacts that the NAO exerts on both variables (Figure 6b,c). Positive NAO phases, and associated
 395 surface buoyancy forcing (Lozier et al., 2008) lead in first instance to negative SSTs (Barrier et al., 2014; Lohmann
 396 et al., 2009) and an almost simultaneous cooling in ESPNA-T700 (Figure 6b). In comparison, on the western side
 397 of the SPNA, positive NAO phases contribute to reduce vertical density stratification, favoring convection and a
 398 more positive LSD index (Robson et al., 2016), which in the models lags the NAO by 2-3 years (Figure 6c). The
 399 fact that correlations between NAO and ESPNA-T700 are weaker than between PC1-LSD and ESPNA-T700
 400 suggests that the ocean might also be playing an additional role (besides the NAO) in controlling the ESPNA
 401 temperatures.



403 **Figure 6:** **a** Lead-lag correlations across the picontrol ensemble between the PC1-LSD index and the vertically
 404 averaged top 700 m temperatures in the eastern subpolar gyre (ESPNA-T700; grey box in Figure 1a). Correlations
 405 are based on 10-year running trends. Significance is assessed as in Figure 2d and indicated with a circle. For positive
 406 lags, PC1-LSD leads. **b-c** The same as in **a** but between the North Atlantic Oscillation (NAO; defined as the
 407 standardised difference in sea level pressure between the closest grid-points to Azores and Reykjavik) and the
 408 ESPNA-T700, and between the NAO and the PC1-LSD, respectively. In these two cases, for negative lags the NAO
 409 leads.

410 The link between PC1-LSD and the ESPNA could be explained through an influence of the PC1-LSD on the
 411 meridional ocean heat transport. This link is now investigated in the two eddy-permitting simulations (Figure 7) and
 412 in the five CMIP5 models for which the ocean heat transport fields are publicly available. In the two high resolution
 413 experiments and two of the CMIP5 ones the decadal trends in the meridional ocean heat transport at 45°N (OHT45)
 414 are strongly linked with those in PC1-LSD. This is a similar relationship to the one previously found in Figure 4
 415 between PC1-LSD and both the AMOC45 and SPGSI, but in this case with PC1-LSD leading with slightly longer
 416 lead time. The other CMIP5 experiments support a weaker, yet significant, link, as well as a longer lag between
 417 OHT45 and PC1-LSD. Altogether, Figure 7a confirms that PC1-LSD is a good precursor of the changes in the
 418 meridional ocean heat transport, although with some differences across models which might reflect a different
 419 representation of certain processes. The contributions of two different processes to this delay are further investigated
 420 in HiGEM, for which OHT had been decomposed online at each time-step into vertical and horizontal heat
 421 transports (as in Bryan, 1969), which can be respectively interpreted as the “overturning” (i.e. characterised by the
 422 zonal mean transport) and “gyre” (i.e. characterised by variations from the zonal mean transport) components
 423 (Robson et al., 2018a). While the overturning contribution ($OHT45_{over}$) increases in phase with the AMOC45,
 424 SPGSI and PC1-LSD changes (Figure 7b), the increase in the gyre component (OHC_{gyre}) starts four years later. That
 425 lag could be the time required in HiGEM for the propagation of mean and/or anomalous temperatures from the
 426 southern to the northern branch of the SPG.



428 **Figure 7:** **a** Lead-lag correlations in a subset of the picontrol experiments between the PC1-LSD index and the
 429 ocean heat transport across the 45°N transect (OHT45N). Note that the ocean heat content is only available for 5
 430 models of the CMIP5 ensemble. Correlations are based on 10-year running trends. **b** The same as in **a** but only in
 431 HiGEM for the different terms of the OHT45N. For positive lags, PC1-LSD leads.

432

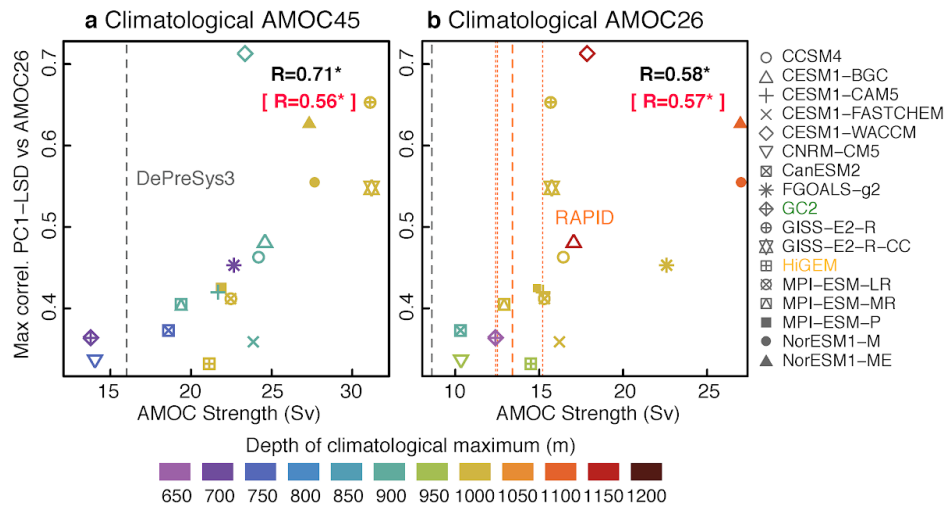
433 4. Characteristics of the inter-model spread in subpolar to subtropical AMOC

434

435 This section investigates which particular climatological model features are linked to the large inter-model spread in
 436 the PC1-LSD vs AMOC26 relationships. The most relevant model features thus identified will improve our process
 437 understanding, and can eventually be used to identify which models are most realistic and, in turn, can deliver more
 438 reliable projections of the future changes in the North Atlantic.

439 [Figure 8](#) shows that models that simulate a stronger and deeper climatological AMOC (both at 45°N and 26°N) tend
 440 to have a stronger correlation between PC1-LSD and the subtropics. All these linear relationships between
 441 climatological AMOC strength and depth and the PC1-LSD vs AMOC26 connectivity are significant at the 95%
 442 confidence level. These climatological AMOC values (without Ekman) can be put in context with those from
 443 RAPID observations and DePreSys3. RAPID observational uncertainties have been considered by including the
 444 mean values over three different non-overlapping periods (i.e. 2004-2007, 2008-2012 and 2013-2016; dotted lines in
 445 [Figure 8](#)). The scatterplots show that the majority of models whose climatological AMOC26 lies within the
 446 RAPID/DePreSys3 climatological spread have a relatively weak link between PC1-LSD and AMOC26, although
 447 some models supporting a strong link are also included or remain close to the RAPID/DePreSys3 values. However,
 448 caution is recommended, e.g., before defining emerging constraints, because model and observations are not directly
 449 comparable for numerous reasons. For example, both RAPID and DePreSys3 cover shorter periods than the
 450 simulations and relate to different background forcing conditions (present day vs preindustrial) which might imply
 451 different mean states (Thornalley et al., 2018). Also, climatological values of the AMOC26 strength are notably
 452 weaker in DePreSys3 than in RAPID, a difference that is not explained by the different temporal periods covered by
 453 each dataset (not shown) and that implies that DePreSys3 might be underestimating too the real AMOC45 strength.
 454 This underestimation might be larger than shown in [Figure 8](#), as evidence suggests RAPID calculations from
 455 mooring arrays might be underestimating the AMOC strength by ~ 1.5 Sv (Sinha et al., 2018).

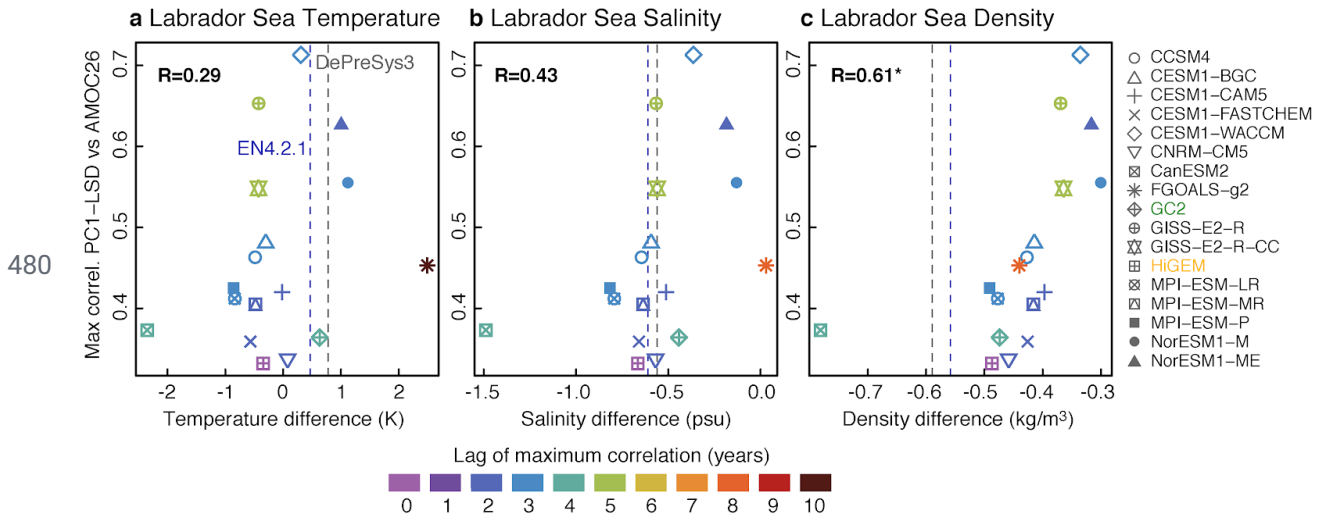
456



457 **Figure 8: a-b** Scatterplot of the maximum cross-correlation value in [Figure 4b](#) between PC1-LSD and AMOC26
 458 against the climatological AMOC45 and AMOC26 means, respectively. All AMOC indices refer to the values after
 459 the Ekman transport signal is removed. The maximum correlations are based on 10-year running trends, and always
 460 happen when PC1-LSD leads the AMOC26 index. Colors indicate the depth at which the climatological AMOC
 461 maximum occurs. The correlation coefficient between the maximum PC1-LSD correlation and the climatological
 462 mean AMOC is shown in the top-left corner in black. In magenta, the analogous correlation but against the depth of
 463 the mean climatological AMOC is shown. The presence of an asterisk indicates that the correlation is significant at
 464 the 95% confidence level. The dashed grey vertical lines mark the climatological AMOC strength value in the
 465 DePreSys3 assimilation run. The orange vertical lines indicate the climatological value from RAPID observations
 466 (Smeed et al., 2018) from 2004 to 2016 (dashed), and in three non-overlapping sub-periods of 4 years (dotted).

467 A potentially important factor behind the inter-model spread in [Figure 4b](#) is the mean density stratification in the
 468 Labrador Sea. [Figure 9](#) suggests that, indeed, the PC1-LSD vs AMOC26 spread is partly influenced by the density
 469 stratification in this region. Models that have a weaker density stratification (here defined as the difference between
 470 the top 100 m, and the average between 500-1000 m), and thus favor deeper convection in the Labrador Sea,

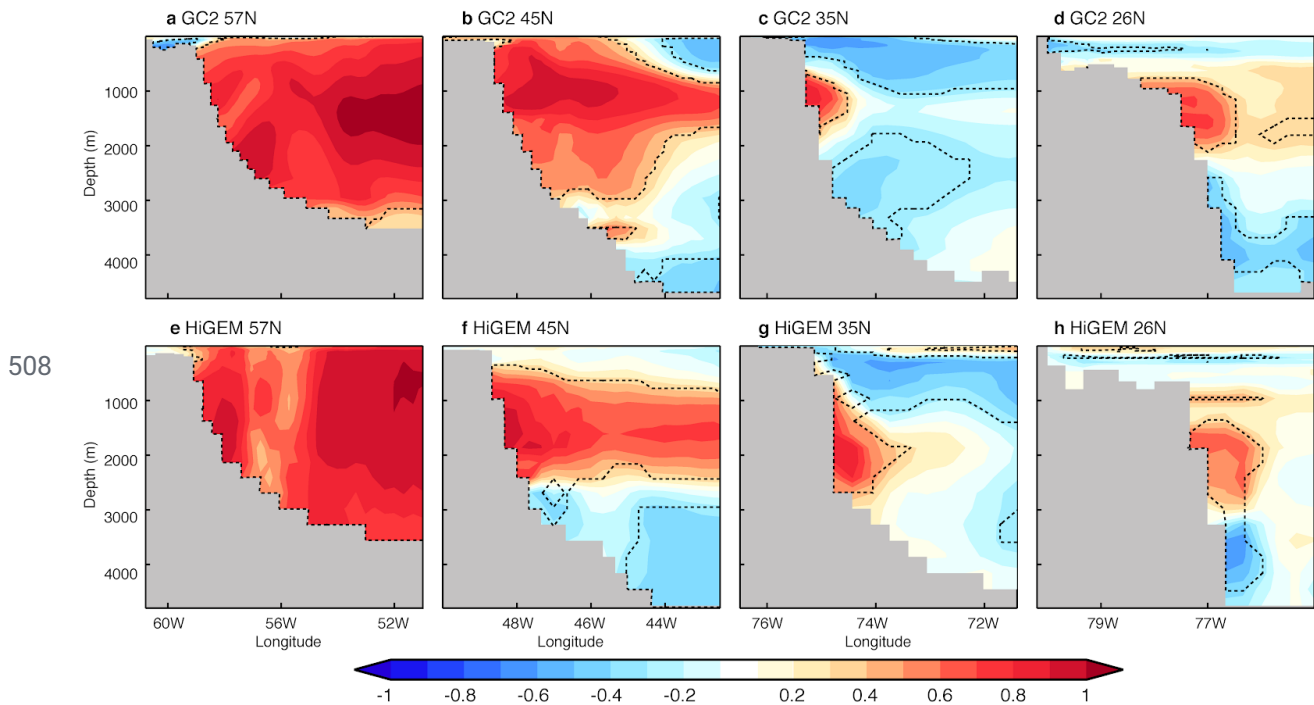
471 generally exhibit a stronger link between PC1-LSD and AMOC26. This result is robust for other stratification
 472 indices based on different depth levels (See [Supplementary Figure 4](#)). Differences in density stratification
 473 across-models can be due to a combination of different factors, from differences in the local buoyancy fluxes (driven
 474 by differences in the atmospheric circulation), to differences in the representation of the Arctic overflows, which are
 475 parameterised in some models (e.g. the CESM family; Danabasoglu et al., 2010), and explicitly resolved in others.
 476 No robust link between the PC1-LSD vs AMOC relationship and both temperature and salinity stratification in the
 477 Labrador Sea has been found. It is also worth mentioning that all models except CanESM2 are more weakly
 478 stratified in the Labrador Sea than the observations (represented herein by the DePreSys3 assimilation run and
 479 EN4.2.1). Hence, the real link of LSD with the AMOC26 may not be as strong as some models suggest.



481 **Figure 9:** a Scatterplot of the maximum cross-correlation value in [Figure 4b](#) between PC1-LSD and AMOC26
 482 (without the Ekman component) against the climatological mean of the Labrador Sea temperature stratification
 483 index (computed as the difference of the vertical means in the levels 0-100 m minus the vertical means in the levels
 484 500-1000 m; see Fig. 1). The maximum correlations are based on 10-year running trends. The correlation coefficient
 485 between the two metrics is shown in the top-left corner. The presence of an asterisk indicates that the correlation is
 486 significant at the 95% confidence level. Colors indicate the lag at which the maximum correlation between
 487 PC1-LSD and AMOC26 is obtained. The grey (blue) vertical lines depict the mean stratification value in the
 488 DePreSys3 assimilation run (EN4.2.1). In both cases, their overlap period is used to compute the climatology (i.e.,
 489 1960-2013). b-c The same as in a but for the Labrador Sea salinity and density (defined as σ_2), respectively.

490 Another key aspect of the PC1-LSD vs AMOC26 connectivity is the western boundary density (WBD). Indeed,
 491 boundary density is critical to the mechanism through which LSD influences the AMOC at lower latitudes. Positive
 492 (negative) LSD anomalies propagate equatorward following this boundary, and as they do so they strengthen
 493 (weaken) the zonal density gradient, triggering a thermal wind response that accelerates (decelerates) the AMOC. In
 494 the following we investigate differences in the propagation of boundary densities across models, and if these
 495 differences can affect the inter-model PC1-LSD vs AMOC26 spread. [Figure 10](#) focuses on the two high-resolution
 496 simulations, where important differences already manifest. It represents the in-phase correlations of PC1-LSD with
 497 the density fields (defined as σ_2) near the western boundary at four different longitudinal transects: 57°N (cutting
 498 across the Labrador Sea), 45°N, 35°N and 26°N. In both models, the depth of the maximum correlation near the
 499 continental shelf is coherent across latitudes. However, in HiGEM these occur at deeper levels (1000 to 3000 m)
 500 compared to GC2 (1000 to 2000 m), and the difference is especially clear at 35°N, where the highest correlations
 501 occur at ~2000 m in HiGEM, while only at 1000 m in GC2. Similar depth differences are also found at 26°N, but

502 with slightly weaker correlations. In addition to the difference in the depth of the maximum correlation between
 503 HiGEM and GC2, there are differences in the vertical structure between the two models. For example, at 35°N in
 504 GC2, density anomalies on the western boundary form a tripole (low correlation above and below the maximum
 505 correlation at ~1000 m), but in HiGEM the density anomalies form a dipole (Figure 10g). We note some differences
 506 in bathymetry at this latitude (which is steeper in HiGEM), which might partly explain some of the differences in
 507 terms of the density correlation structure.

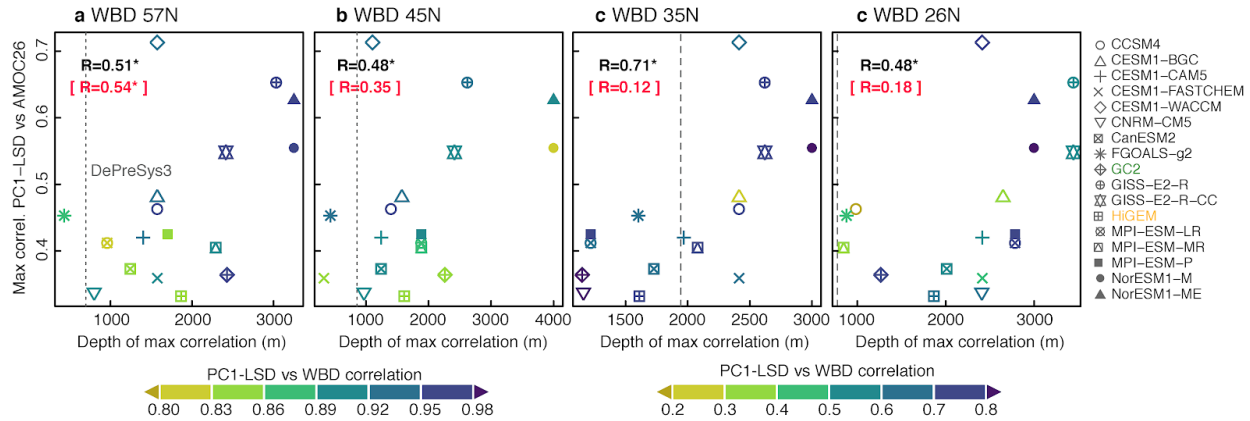


509 **Figure 10:** a In-phase correlation in GC2 between the PC1-LSD index and the density fields across a zonal section
 510 at 57°N located in the vicinity of the western Atlantic boundary. Thin dashed contours enclose areas where the
 511 correlation significance exceeds the 95% confidence level. Correlations are based on 10-year running trends. **b-d**
 512 The same as in *a* but for zonal sections at 45°N, 35°N and 26°N. **d-h** The same as in *a-d* but for HiGEM.

513

514 [Figure 11](#) shows that the diversity in the depth of these boundary densities is even more evident when including the
 515 CMIP5 models. The depth of the maximum correlation between PC1-LSD and the western boundary density at the
 516 four latitudinal sections relates linearly (and significantly at the 95% confidence level) across models with their
 517 PC1-LSD vs AMOC26 correlation. In this case, models exhibiting maximum correlations with the WBDs at deeper
 518 levels generally show stronger links between PC1-LSD and the subtropical AMOC. In DePreSys, our
 519 observationally-constrained reference (dashed grey lines in [Figure 11](#)), these maximum correlations tend to occur at
 520 relatively shallow levels when compared with the multi-model ensemble. We have also checked if models with
 521 stronger correlations with the WBDs (as represented by the PC1-LSD and WBD maximum correlations at every
 522 latitudinal section) also support a stronger link between the PC1-LSD and the AMOC, but this linearity assumption
 523 only holds true at 57°N (correlations in magenta in [Figure 11](#)). This suggests that the depth along which WBDs
 524 propagate southward, and/or the vertical structure of anomalies, are the key aspects to understand and potentially
 525 narrow down the spread.

526



527 **Figure 11:** a Scatterplot of the maximum cross-correlations value in [Figure 4b](#) between PC1-LSD and AMOC26
 528 (without the Ekman component) against the depth at which the maximum correlations at any lag between PC1-LSD
 529 and the WBD at 57°N occur. The maximum correlations are based on 10-year running trends. The correlation
 530 coefficient between the two metrics is shown in black the top-left corner. Likewise, another correlation coefficient in
 531 magenta is shown, computed between the PC1-LSD and AMOC26 maximum correlation and the PC1-LSD and
 532 WBD at 57°N maximum correlation. The presence of an asterisk indicates that the correlation is significant at the
 533 95% confidence level. Colors indicate the maximum correlation between PC1-LSD and the WBD. The grey vertical
 534 lines depict the corresponding depth of maximum correlation for the DePreSys3 assimilation run. **b-d** The same as
 535 in **a** but for the WBD at 45, 35 and 26°N, respectively.

536

537 5. Conclusions and discussion

538

539 This article has explored, in a multi-model context, the linkages between subsurface density in the subpolar North
 540 Atlantic (SPNA) and the ocean circulation further south. In particular, it has explored the role of Labrador Sea
 541 density (LSD) in driving Western Boundary Density anomalies (WBD) and the ocean circulation, and the impact on
 542 upper ocean temperature changes in the SPNA. The analysis was based on two control simulations with
 543 eddy-permitting models, a preindustrial one with HadGEM3-GC2 and a present day one with HiGEM, and on 20
 544 CMIP5 preindustrial experiments. Furthermore, where possible these characteristic model features have been
 545 computed in observational datasets, as well as in a simulation assimilating observations. The major findings are
 546 listed below:

547

- 548 - All the simulations show clear multidecadal variability in Labrador Sea density. There is also a close link
 549 between LSD and the strength of the subpolar Atlantic Ocean circulation, with positive density anomalies
 550 leading to a strengthening of the Atlantic Meridional Overturning Circulation (AMOC) at 45°N and the
 551 Subpolar Gyre (SPG) circulation.
- 552 - The relationship between anomalous LSD and the strength of the AMOC at 26°N - the latitude of the
 553 RAPID array measurements - is also positive in the simulations, but there are significant inter-model
 554 differences, both in the strength of the relationship and the lag of maximum correlation. This uncertainty
 555 implies that the connectivity of LSD with the subtropics and latitudinal AMOC coherence is
 556 model-dependent.
- 557 - The connectivity between anomalies in LSD and AMOC at 26°N is sensitive to different model features,
 558 including the strength and depth of the climatological AMOC maximum, the mean density stratification in
 559 the Labrador Sea, and the depths at which the LSD propagates southward along the western boundary.

560 Stronger LSD connectivity with the subtropics tends to occur in models with a stronger and deeper AMOC,
561 weaker Labrador Sea stratification and western boundary density propagating at deeper levels.
562 - Observationally derived constraints of the model based relationships tend to suggest that the link between
563 LSD and the subtropical AMOC is weak. This suggests that observations of AMOC via RAPID may not be
564 representative of the basin wide buoyancy forced AMOC variability. However, caution is advised because
565 simulations and observations are not directly comparable, and so significant uncertainty remains in
566 constraining the relationship between LSD and subtropical AMOC.
567 - The multi-model ensemble does also support a significant lagged relationship between LSD and the upper
568 ocean temperature in the eastern SPNA, in line with previous studies linking LSD to the recently observed
569 changes in the North Atlantic. However, models disagree regarding the strength of the link (correlations
570 between 0.3-0.7), and the maximum lag (3 to 10 years).

571
572 We have shown that, in coupled climate models at least, subsurface density anomalies in the western SPNA are an
573 important predictor of the wider North Atlantic ocean circulation and upper ocean temperature in the SPNA. This
574 importance on the ocean circulation is especially clear at the latitudes of the SPNA itself. Given the important role
575 of the wind in driving lower latitude AMOC anomalies, and the range of processes by which wind can act on the
576 AMOC (Duchez et al., 2014b, 2014a; Kanzow et al., 2010; Polo et al., 2014; Zhao and Johns, 2014) it is not
577 surprising that the relationship between LSD and AMOC at 26°N is much weaker. Nevertheless, the reasons behind
578 the large spread in these relationships across models is not so clear.

579 We have tried to constrain this uncertainty by looking at a range of observed metrics that may explain the spread in
580 the correlation strength, including the density anomalies on the western boundary, the stratification of the Labrador
581 Sea, and the mean-AMOC strength. Overall, these constraints point to a relatively weak relationship between LSD
582 and AMOC at 26°N on decadal timescales (i.e. $r \sim 0.4$) in the real world. However, there are many reasons why this
583 number is still very uncertain, and further work is needed to assess its validity. A caveat of this study is that the
584 simulations and observation-based datasets employed are not directly comparable, as they differ in the background
585 radiative forcing levels, the length of the period used to compute the climatologies, and even the way some indices,
586 like the AMOC, are computed. We also recognise that there is large uncertainty within the observationally derived
587 metrics. For instance, the assimilation run in DePreSys3, which is used to constrain relationships, clearly
588 underestimates the mean AMOC strength at 26°N with respect to RAPID (see [Figure 8b](#)) and, therefore, might be
589 also underestimating the AMOC at higher latitudes. Our findings might also be limited by model deficiencies. There
590 is emerging evidence that current models underestimate AMOC and North Atlantic variability on decadal timescales
591 (Roberts et al., 2013; Cheung et al., 2017;), which can degrade decadal predictability in the region and even lead to
592 overly weak linkages between the AMOC and the AMV (Yan et al., 2018). The AMV is indeed a mode of
593 variability that also shows important differences across models, in different aspects like its periodicity, amplitude,
594 spatial structure and climate footprints (Medhaug and Furevik, 2011; Zhang and Wang 2013; Kavvada et al., 2013),
595 inter-model differences that could be partly connected with those herein reported for the PC1-LSD vs AMOC
596 relationships. Models also tend to generally underestimate the depth of the return flow, and this may still affect how
597 density anomalies project on the basin-wide AMOC. It has also been argued that ocean-only models produce too
598 much deep water in the western basin and Labrador Sea (i.e., Li et al., 2019), and recent observations even challenge
599 the prevailing view from models that Labrador Sea convection dominates the AMOC variability (Koenigk and
600 Brodeau, 2017), suggesting that the key deep water formation occurs in the Irminger Sea, a few hundred kilometers
601 north east of the Labrador Sea (Lozier et al., 2019). Therefore, further in-depth study is warranted to narrow down
602 the uncertainty in the real AMOC and PC1-LSD relationship.

603 Most of the models considered in this study have relatively coarse resolution, including non-eddy oceans (\geq
604 $1^\circ \times 1^\circ$), which means that they might be missing some key dynamics for the AMOC (Johnson et al., 2019) that could
605 be important to represent realistic linkages. The current analysis also includes two models at eddy-permitting

606 resolution (HadGEM3-GC2 and HiGEM), whose relationships lie within the spread of those in the coarser models.
607 However, it could be that higher resolution is needed (e.g. enabling meso-scale eddies in subpolar latitudes) to
608 identify substantial differences (Hirschi et al., 2020; Johnson et al., 2019). A recent analysis based on
609 HadGEM3-GC3.1 (a later version of HadGEM3-GC2) configured at different horizontal resolutions has shown that
610 long-standing model biases affecting the North Atlantic are reduced at eddy-resolving resolution ($1/12^\circ \times 1/12^\circ$ in
611 the ocean), and that the strength of the AMOC, the boundary currents and the northward heat transport is higher than
612 for the coarser resolutions (Hirschi et al., 2020; Roberts et al., 2019). High resolution coupled models also generally
613 support the new view from OSNAP observations in which the largest fraction of AMOC variability (on sub annual
614 to decadal timescales) originates at the eastern SPNA (Hirschi et al., 2020). Eddy-resolving resolutions have also
615 been shown in a multi-model study (Roberts et al., 2020) to represent the AMOC response at 26°N differently in
616 future projections, leading to stronger declines than in non-eddying simulations, declines mostly associated with a
617 weakening in the Florida Current. Roberts et al. (2020) also compares the meridional coherence of the AMOC,
618 which does not seem to be resolution-dependent, a result that is in line with another multi-model comparison
619 between non-eddying and eddy-permitting simulations (Li et al., 2019).

620 Despite the current limitations in the models considered for this study, it is important to highlight that they provide a
621 rather consistent picture of a chain of relationships in the North Atlantic that is able to explain some of the recent
622 observed trends (Robson et al. 2016). This paper has broadly characterized this behaviour, and highlighted the
623 uncertainty. These relationships are also consistent with the mechanisms proposed by Yeager and Robson (2017) to
624 explain high levels of predictive skill in the SPNA on decadal timescales. Our analysis has also helped to identify
625 specific metrics (such as LSD stratification and the depth of the boundary density) that could be used as emergent
626 constraints for future projections, i.e. to subset the simulations expected to more realistically represent the future
627 changes in the region. Having a more realistic subpolar gyre stratification at present day conditions has been shown
628 in CMIP5 simulations to increase the probability of a future collapse in convection (Sgubin et al., 2017), that would
629 lead to a widespread SPG cooling. It remains to be tested if similar conclusions can be drawn from eddy-resolving
630 simulations.

631 **Code availability.** The main scripts used in the analysis and other supporting information that may be useful to
632 reproduce the results of this article are archived at the Barcelona Supercomputing Center and will be shared upon
633 request by the corresponding author.

634 **Data availability.** Outputs from the CMIP5 simulations can be downloaded from the corresponding ESGF node:
635 <https://esgf-node.llnl.gov/projects/cmip5/>. EN4 observations used in this study correspond to version 2.1 of the
636 dataset, available at <https://www.metoffice.gov.uk/hadobs/en4/download-en4-2-1.html>. Outputs from the GC2,
637 HiGEM and DePreSys3 simulations are available upon request to the corresponding author.

638 **Author contributions.** P. O., J. R. and R. S. conceived the study, which was later discussed and refined with the
639 other co-authors. M. M. downloaded and processed the CMIP5 data, computing the main climate indices. P. O. led
640 the analysis, and together with J. R. prepared the manuscript with contributions from all co-authors.

641 **Competing interests.** The authors declare that they have no conflict of interest.

642 **Acknowledgements.** We thank the UK Met Office for providing the model data of GC2 used in this study, and all
643 the research centers that contributed to CMIP5 and made their data available. This work was largely supported by
644 the NERC Projects “Dynamics and Predictability of the Atlantic Meridional Overturning and Climate Project”
645 (DYNAMOC, NE/ M005127/1) and “Wider Impacts of Subpolar North Atlantic Decadal Variability on the Ocean
646 and Atmosphere” (WISHBONE, NE/T013516/1). P. O. work was additionally supported by the Spanish Ministry of
647 Economy, Industry and Competitiveness through the Ramon y Cajal grant RYC-2017-22772. J. R. was additionally

648 supported by the NERC ACSIS program and R. S. by NERC via the National Centre for Atmospheric Science
649 (NCAS).

650 **References**

651

652 Ba, J., Keenlyside, N.S., Park, W., Latif, M., Hawkins, E., Ding, H.: A mechanism for Atlantic
653 multidecadal variability in the Kiel Climate Model, *Clim. Dyn.*, 41, 2133–2144, 2013.

654

655 Baehr, J., Hirschi, J., Beismann, J.-O. and Marotzke, J.: Monitoring the meridional overturning circulation
656 in the North Atlantic: A model-based array design study, *J. Mar. Res.*, 62(3), 283–312,
657 doi:10.1357/0022240041446191, 2004.

658

659 Barrier, N., Cassou, C., Deshayes, J. and Treguier, A.-M.: Response of North Atlantic Ocean Circulation to
660 Atmospheric Weather Regimes, *J. Phys. Oceanogr.*, 44(1), 179–201, doi:10.1175/JPO-D-12-0217.1, 2014.

661

662 Bingham, R. J. and Hughes, C. W.: Geostrophic dynamics of meridional transport variability in the
663 subpolar North Atlantic, *J. Geophys. Res. Oceans*, 114(C12), doi:10.1029/2009JC005492, 2009.

664

665 Bretherton, C. S., Widmann, M., Dymnikov, V. P., Wallace, J. M. and Blad??, I.: The effective number of
666 spatial degrees of freedom of a time-varying field, *J. Clim.*, 12(7), 1990–2009,
667 doi:10.1175/1520-0442(1999)012<1990:TENOSD>2.0.CO;2, 1999.

668

669 Bryan, K.: Climate and the Ocean Circulation: III. The Ocean Model, *Mon. Weather Rev.*, 97(11),
670 806–827, doi:10.1175/1520-0493(1969)097<0806:CATOC>2.3.CO;2, 1969.

671

672 Caesar, L., Rahmstorf, S., Robinson, A., Feulner, G. and Saba, V.: Observed fingerprint of a weakening
673 Atlantic Ocean overturning circulation, *Nature*, 556(7700), 191–196, doi:10.1038/s41586-018-0006-5, 2018.

674

675 Cheung, A. H., Mann, M. E., Steinman, B. A., Frankcombe, L. M., England, M. H., & Miller, S. K.:
676 Comparison of Low-Frequency Internal Climate Variability in CMIP5 Models and Observations, *Journal of Climate*,
677 30(12), 4763–4776, 2017.

678

679 Danabasoglu, G.: On multidecadal variability of the Atlantic meridional overturning circulation in the
680 community climate system model version 3, *J. Clim.*, 21, 5524–5544, doi:10.1175/2008JCLI2019.1, 2008.

681

682 Delworth, T. L., & Zeng, F.: The Impact of the North Atlantic Oscillation on Climate through Its Influence
683 on the Atlantic Meridional Overturning Circulation, *Journal of Climate*, 29(3), 941–962, 2016.

684

685 Desbruyères, D. G., Mercier, H., Maze, G. and Danialt, N.: Surface predictor of overturning circulation
686 and heat content change in the subpolar North Atlantic, *Ocean Sci*, 15(3), 809–817, doi:10.5194/os-15-809-2019,
687 2019.

688

689 Dong, B. and Sutton, R. T.: Mechanism of interdecadal thermohaline circulation variability in a coupled
690 ocean-atmosphere GCM, *J. Clim.*, 18(1964), 1117–1135, doi:10.1175/JCLI3328.1, 2005.

691

692 Duchez, A., Hirschi, J. J.-M., Cunningham, S. A., Blaker, A. T., Bryden, H. L., de Cuevas, B., Atkinson, C.
693 P., McCarthy, G. D., Frajka-Williams, E., Rayner, D., Smeed, D. and Mizielinski, M. S.: A New Index for the
694 Atlantic Meridional Overturning Circulation at 26°N, *J. Clim.*, 27(17), 6439–6455, doi:10.1175/JCLI-D-13-00052.1,
695 2014a.

696

697 Duchez, A., Frajka-Williams, E., Castro, N., Hirschi, J. and Coward, A.: Seasonal to interannual variability
698 in density around the Canary Islands and their influence on the Atlantic meridional overturning circulation at 26°N,
699 *J. Geophys. Res. Oceans*, 119(3), 1843–1860, doi:10.1002/2013JC009416, 2014b.

700
701 Ducheze, A., Frajka-Williams, E., Josey, S. A., Evans, D. G., Grist, J. P., Marsh, R., McCarthy, G. D., Sinha,
702 B., Berry, D. I. and Hirschi, J. J.-M.: Drivers of exceptionally cold North Atlantic Ocean temperatures and their link
703 to the 2015 European heat wave, *Environ. Res. Lett.*, 11(7), 074004, doi:10.1088/1748-9326/11/7/074004, 2016.
704
705 Dunstone, N., Smith, D., Scaife, A., Hermanson, L., Eade, R., Robinson, N., Andrews, M. and Knight, J.:
706 Skilful predictions of the winter North Atlantic Oscillation one year ahead, *Nat. Geosci.*, 9, 809, 2016.
707
708 Flato, G., Marotzke, J., Abiodun, B., Braconnot, P., Chou, S. C., Collins, W., Cox, P., Driouech, F., Emori,
709 S., Eyring, V., Forest, C., Gleckler, P., Guilyardi, E., Jakob, C., Kattsov, V., Reason, C. and Rummukainen, M.:
710 IPCC 2013 AR5 - Chapter 9: Evaluation of Climate Models, *Clim. Change 2013 Phys. Sci. Basis Contrib. Work.*
711 *Group Fifth Assess. Rep. Intergov. Panel Clim. Change*, doi:10.1017/CBO9781107415324, 2013.
712
713 Fröb, F., Olsen, A., Våge, K., Moore, G. W. K., Yashayaev, I., Jeansson, E. and Rajasakaren, B.: Irminger
714 Sea deep convection injects oxygen and anthropogenic carbon to the ocean interior, *Nat. Commun.*, 7, 13244, 2016.
715
716 Good, S. A., Martin, M. J. and Rayner, N. A.: EN4: quality controlled ocean temperature and salinity
717 profiles and monthly objective analyses with uncertainty estimates, *J Geophys Res*, 118, 6704–6716, 2013.
718
719 Grist, J. P., Josey, S. a., Marsh, R., Kwon, Y. O., Bingham, R. J. and Blaker, A. T.: The surface-forced
720 overturning of the North Atlantic: Estimates from modern era atmospheric reanalysis datasets, *J. Clim.*, 27,
721 3596–3618, doi:10.1175/JCLI-D-13-00070.1, 2014.
722
723 Häkkinen, S. and Rhines, P. B.: Decline of subpolar North Atlantic circulation during the 1990s., *Science*,
724 304(2004), 555–559, doi:10.1126/science.1094917, 2004.
725
726 Hermanson, L., Eade, R., Robinson, N. H., Dunstone, N. J., Andrews, M. B., Knight, J. R., Scaife, A. A.
727 and Smith, D. M.: Forecast cooling of the Atlantic subpolar gyre and associated impacts, *Geophys. Res. Lett.*,
728 41(14), 5167–5174, doi:10.1002/2014GL060420, 2014.
729
730 Hirschi, J. J.-M., Barnier, B., Böning, C., Biastoch, A., Blaker, A. T., Coward, A., Danilov, S., Drijfhout, S.,
731 Getzlaff, K., Griffies, S. M., Hasumi, H., Hewitt, H., Iovino, D., Kawasaki, T., Kiss, A. E., Koldunov, N.,
732 Marzocchi, A., Mecking, J. V., Moat, B., Molines, J.-M., Myers, P. G., Penduff, T., Roberts, M., Treguier, A.-M.,
733 Sein, D. V., Sidorenko, D., Small, J., Spence, P., Thompson, L., Weijer, W. and Xu, X.: The Atlantic meridional
734 overturning circulation in high resolution models, *J. Geophys. Res. Oceans*, n/a(n/a), e2019JC015522,
735 doi:10.1029/2019JC015522, 2020.
736
737 Hodson, D. L. R. and Sutton, R. T.: The impact of resolution on the adjustment and decadal variability of
738 the Atlantic meridional overturning circulation in a coupled climate model, *Clim. Dyn.*, 39(12), 3057–3073,
739 doi:10.1007/s00382-012-1309-0, 2012.
740
741 Holliday, N. P., Bersch, M., Berx, B., Chafik, L., Cunningham, S., Florindo-López, C., Hátún, H., Johns,
742 W., Josey, S. A., Larsen, K. M. H., Mulet, S., Oltmanns, M., Reverdin, G., Rossby, T., Thierry, V., Valdimarsson, H.
743 and Yashayaev, I.: Ocean circulation causes the largest freshening event for 120 years in eastern subpolar North
744 Atlantic, *Nat. Commun.*, 11(1), 585, doi:10.1038/s41467-020-14474-y, 2020.
745
746 Jackson, L. C., Peterson, K. A., Roberts, C. D. and Wood, R. A.: Recent slowing of Atlantic overturning
747 circulation as a recovery from earlier strengthening, *Nat. Geosci.*, 9(7), 518–522, 2016.
748
749 Jackson, L. C., Dubois, C., Forget, G., Haines, K., Harrison, M., Iovino, D., Köhl, A., Mignac, D., Masina,
750 S., Peterson, K. A., Piecuch, C. G., Roberts, C. D., Robson, J., Storto, A., Toyoda, T., Valdivieso, M., Wilson, C.,
751 Wang, Y. and Zuo, H.: The Mean State and Variability of the North Atlantic Circulation: A Perspective From Ocean
752 Reanalyses, *J. Geophys. Res. Oceans*, 124(12), 9141–9170, doi:10.1029/2019JC015210, 2019.
753

754 Johnson, H. L., Cessi, P., Marshall, D. P., Schloesser, F. and Spall, M. A.: Recent Contributions of Theory
755 to Our Understanding of the Atlantic Meridional Overturning Circulation, *J. Geophys. Res. Oceans*, 124(8),
756 5376–5399, doi:10.1029/2019JC015330, 2019.

757

758 Josey, S. A., Hirschi, J. J.-M., Sinha, B., Ducez, A., Grist, J. P. and Marsh, R.: The Recent Atlantic Cold
759 Anomaly: Causes, Consequences, and Related Phenomena, *Annu. Rev. Mar. Sci.*, 10(1), 475–501,
760 doi:10.1146/annurev-marine-121916-063102, 2018.

761

762 Joyce, T. M., and Zhang, R.: On the Path of the Gulf Stream and the Atlantic Meridional Overturning
763 Circulation, *J. Clim.*, 23, 3146–3154, 2010.

764

765 Jungclauss, J. H., Haak, H., Latif, M. and Mikolajewicz, U.: Arctic-North Atlantic interactions and
766 multidecadal variability of the meridional overturning circulation, *J. Clim.*, 18(19), 4013–4031,
767 doi:10.1175/JCLI3462.1, 2005.

768

769 Kanzow, T., Cunningham, S. A., Johns, W. E., Hirschi, J. J.-M., Marotzke, J., Baringer, M. O., Meinen, C.
770 S., Chidichimo, M. P., Atkinson, C., Beal, L. M., Bryden, H. L. and Collins, J.: Seasonal Variability of the Atlantic
771 Meridional Overturning Circulation at 26.5°N, *J. Clim.*, 23(21), 5678–5698, doi:10.1175/2010JCLI3389.1, 2010.

772

773 Karspeck, A. R., Stammer, D., Köhl, A., Danabasoglu, G., Balmaseda, M., Smith, D. M., Fujii, Y., Zhang,
774 S., Giese, B., Tsujino, H. and Rosati, A.: Comparison of the Atlantic meridional overturning circulation between
775 1960 and 2007 in six ocean reanalysis products, *Clim. Dyn.*, Published Online-Published Online,
776 doi:10.1007/s00382-015-2787-7, 2015.

777

778 Katsman, C. A., Drijfhout, S. S., Dijkstra, H. A. and Spall, M. A.: Sinking of Dense North Atlantic Waters
779 in a Global Ocean Model: Location and Controls, *J. Geophys. Res. Oceans*, 123(5), 3563–3576,
780 doi:10.1029/2017JC013329, 2018.

781

782 Kavvada, A., Ruiz-Barradas, A. and Nigam, S.: AMO’s structure and climate footprint in observations and
783 IPCC AR5 climate simulations, *Clim. Dyn.*, 41, 1345–1364, 2013.

784

785 Kim, W. M., Yeager, S. and Danabasoglu, G.: Atlantic Multidecadal Variability and Associated Climate
786 Impacts Initiated by Ocean Thermohaline Dynamics, *J. Clim.*, 33(4), 1317–1334, doi:10.1175/JCLI-D-19-0530.1,
787 2020.

788

789 Knight, J. R., Allan, R. J., Folland, C. K., Vellinga, M. and Mann, M. E.: A signature of persistent natural
790 thermohaline circulation cycles in observed climate, *Geophys. Res. Lett.*, 32, 1–4, doi:10.1029/2005GL024233,
791 2005.

792

793 Knight, J. R., Folland, C. K. and Scaife, A. a.: Climate impacts of the Atlantic multidecadal oscillation,
794 *Geophys. Res. Lett.*, 33, 1–4, doi:10.1029/2006GL026242, 2006.

795

796 Koenigk, T. and Brodeau, L.: Arctic climate and its interaction with lower latitudes under different levels of
797 anthropogenic warming in a global coupled climate model, *Clim. Dyn.*, 49(1), 471–492,
798 doi:10.1007/s00382-016-3354-6, 2017.

799

800 Langehaug, H. R., Rhines, P. B., Eldevik, T., Mignot, J. and Lohmann, K.: Water mass transformation and
801 the North Atlantic Current in three multicentury climate model simulations, *J. Geophys. Res. Oceans*, 117(C11),
802 doi:10.1029/2012JC008021, 2012.

803

804 Li, F., Lozier, M. S., Danabasoglu, G., Holliday, N. P., Kwon, Y.-O., Romanou, A., Yeager, S. G. and
805 Zhang, R.: Local and Downstream Relationships between Labrador Sea Water Volume and North Atlantic
806 Meridional Overturning Circulation Variability, *J. Clim.*, 32(13), 3883–3898, doi:10.1175/JCLI-D-18-0735.1, 2019.

807

808 Lohmann, K., Drange, H. and Bentsen, M.: Response of the North Atlantic subpolar gyre to persistent
809 North Atlantic oscillation like forcing, *Clim. Dyn.*, 32, 273–285, doi:10.1007/s00382-008-0467-6, 2009.
810

811 Lozier, M. S., Leadbetter, S., Williams, R. G., Roussenov, V., Reed, M. S. C. and Moore, N. J.: The spatial
812 pattern and mechanisms of heat-content change in the North Atlantic., *Science*, 319, 800–803,
813 doi:10.1126/science.1146436, 2008.
814

815 Lozier, M. S., Li, F., Bacon, S., Bahr, F., Bower, A. S., Cunningham, S. A., de Jong, M. F., de Steur, L.,
816 deYoung, B., Fischer, J., Gary, S. F., Greenan, B. J. W., Holliday, N. P., Houk, A., Houpert, L., Inall, M. E., Johns,
817 W. E., Johnson, H. L., Johnson, C., Karstensen, J., Koman, G., Le Bras, I. A., Lin, X., Mackay, N., Marshall, D. P.,
818 Mercier, H., Oltmanns, M., Pickart, R. S., Ramsey, A. L., Rayner, D., Straneo, F., Thierry, V., Torres, D. J.,
819 Williams, R. G., Wilson, C., Yang, J., Yashayaev, I. and Zhao, J.: A sea change in our view of overturning in the
820 subpolar North Atlantic, *Science*, 363(6426), 516, doi:10.1126/science.aau6592, 2019.
821

822 McCarthy, G. D., Haigh, I. D., Hirschi, J. J.-M., Grist, J. P. and Smeed, D. A.: Ocean impact on decadal
823 Atlantic climate variability revealed by sea-level observations., *Nature*, 521(7553), 508–510,
824 doi:10.1038/nature14491, 2015.
825

826 Medhaug, I. and Furevik, T.: North Atlantic 20th century multidecadal variability in coupled climate
827 models: sea surface temperature and ocean overturning circulation, *Ocean Sci.*, 7, 389–404, 2011.
828

829 Menary, M. B., Hodson, D. L. R., Robson, J. I., Sutton, R. T., Wood, R. A. and Hunt, J. A.: Exploring the
830 impact of CMIP5 model biases on the simulation of North Atlantic decadal variability, *Geophys. Res. Lett.*, 42(14),
831 5926–5934, doi:10.1002/2015GL064360, 2015.
832

833 Moat, B. I., Sinha, B., Josey, S. A., Robson, J., Ortega, P., Sévellec, F., Holliday, N. P., McCarthy, G. D.,
834 New, A. L. and Hirschi, J. J.-M.: Insights into Decadal North Atlantic Sea Surface Temperature and Ocean Heat
835 Content Variability from an Eddy-Permitting Coupled Climate Model, *J. Clim.*, 32(18), 6137–6161,
836 doi:10.1175/JCLI-D-18-0709.1, 2019.
837

838 Monerie, P.-A., Robson, J., Dong, B., Dieppois, B., Pohl, B. and Dunstone, N.: Predicting the seasonal
839 evolution of southern African summer precipitation in the DePreSys3 prediction system, *Clim. Dyn.*, 52(11),
840 6491–6510, doi:10.1007/s00382-018-4526-3, 2019.
841

842 Nigam, S., Ruiz-Barradas, A., and Chafik, L.: Gulf Stream Excursions and Sectional Detachments Generate
843 the Decadal Pulses in the Atlantic Multidecadal Oscillation, *J. Clim.*, 31, 2853–2870, 2018.
844

845 Ortega, P., Hawkins, E. and Sutton, R.: Processes governing the predictability of the Atlantic meridional
846 overturning circulation in a coupled GCM, *Clim. Dyn.*, 37(9–10), doi:10.1007/s00382-011-1025-1, 2011.
847

848 Ortega, P., Mignot, J., Swingedouw, D., Sévellec, F. and Guilyardi, E.: Reconciling two alternative
849 mechanisms behind bi-decadal variability in the North Atlantic, *Prog. Oceanogr.*, 137,
850 doi:10.1016/j.pocean.2015.06.009, 2015.
851

852 Ortega, P., Robson, J., Sutton, R. T. and Andrews, M. B.: Mechanisms of decadal variability in the
853 Labrador Sea and the wider North Atlantic in a high-resolution climate model, *Clim. Dyn.*, 49(7–8),
854 doi:10.1007/s00382-016-3467-y, 2017.
855

856 Pickart, R. S. and Spall, M. a.: Impact of Labrador Sea Convection on the North Atlantic Meridional
857 Overturning Circulation, *J. Phys. Oceanogr.*, 37(1993), 2207–2227, doi:10.1175/JPO3178.1, 2007.
858

859 Piecuch, C. G., Ponte, R. M., Little, C. M., Buckley, M. W. and Fukumori, I.: Mechanisms underlying
860 recent decadal changes in subpolar North Atlantic Ocean heat content, *J. Geophys. Res. Oceans*, 122(9), 7181–7197,
861 doi:10.1002/2017JC012845, 2017.

862
863 Polo, I., Robson, J., Sutton, R. and Balmaseda, M. A.: The Importance of Wind and Buoyancy Forcing for
864 the Boundary Density Variations and the Geostrophic Component of the AMOC at 26°N, *J. Phys. Oceanogr.*, 44(9),
865 2387–2408, doi:10.1175/JPO-D-13-0264.1, 2014.

866
867 Polyakov, I.V., Alexeev, V.A., Bhatt, U.S., Polyakova, E. I., Zhang, X.: North Atlantic warming: patterns of
868 long-term trend and multidecadal variability, *Clim. Dyn.* 34, 439–457, 2010.

869
870 Rahmstorf, S., Box, J. E., Feulner, G., Mann, M. E., Robinson, A., Rutherford, S. and Schaffernicht, E. J.:
871 Exceptional twentieth-century slowdown in Atlantic Ocean overturning circulation, *Nat. Clim. Change*, 5(5),
872 475–480, doi:10.1038/nclimate2554, 2015.

873
874 Reintges, A., Martin, T., Latif, M. and Keenlyside, N. S.: Uncertainty in twenty-first century projections of
875 the Atlantic Meridional Overturning Circulation in CMIP3 and CMIP5 models, *Clim. Dyn.*, 49(5), 1495–1511,
876 doi:10.1007/s00382-016-3180-x, 2017.

877
878 Reverdin, G.: North Atlantic subpolar Gyre surface variability (1895-2009), *J. Clim.*, 23, 4571–4584,
879 doi:10.1175/2010JCLI3493.1, 2010.

880
881 Roberts, C. D., Garry, F. K. and Jackson, L. C.: A Multimodel Study of Sea Surface Temperature and
882 Subsurface Density Fingerprints of the Atlantic Meridional Overturning Circulation, *J. Clim.*, 26(22), 9155–9174,
883 doi:10.1175/JCLI-D-12-00762.1, 2013.

884
885 Roberts, M. J., Baker, A., Blockley, E. W., Calvert, D., Coward, A., Hewitt, H. T., Jackson, L. C.,
886 Kuhlbrodt, T., Mathiot, P., Roberts, C. D., Schiemann, R., Seddon, J., Vanni ere, B. and Vidale, P. L.: Description of
887 the resolution hierarchy of the global coupled HadGEM3-GC3.1 model as used in CMIP6 HighResMIP
888 experiments, *Geosci Model Dev*, 12(12), 4999–5028, doi:10.5194/gmd-12-4999-2019, 2019.

889
890 Roberts, M. J., Jackson, L. C., Roberts, C. D., Meccia, V., Docquier, D., Koenigk, T., Ortega, P.,
891 Moreno-Chamarro, E., Bellucci, A., Coward, A., Drijfhout, S., Exarchou, E., Gutjahr, O., Hewitt, H. T., Iovino, D.,
892 Lohmann, K., Schiemann, R., Seddon, J., Terray, L., Xu, X., Zhang, Q., Chang, P., Yeager, S. G., Castruccio, F.,
893 Zhang, S. and Wu, L.: Sensitivity of the Atlantic Meridional Overturning Circulation to Model Resolution in CMIP6
894 HighResMIP Simulations and Implications for Future Changes, JAMES, Published online, 2020.

895
896 Robson, J., Lohmann, K., Smith, D. and Palmer, M. D.: Causes of the rapid warming of the North Atlantic
897 Ocean in the mid-1990s, *J. Clim.*, 25(2008), 4116–4134, doi:10.1175/JCLI-D-11-00443.1, 2012.

898
899 Robson, J., Sutton, R. and Smith, D.: Predictable climate impacts of the decadal changes in the ocean in the
900 1990s, *J. Clim.*, 26, 6329–6339, doi:10.1175/JCLI-D-12-00827.1, 2013.

901
902 Robson, J., Hodson, D., Hawkins, E. and Sutton, R.: Atlantic overturning in decline?, *Nat. Geosci.*, 7(1),
903 2–3, doi:10.1038/ngeo2050, 2014.

904
905 Robson, J., Ortega, P. and Sutton, R.: A reversal of climatic trends in the North Atlantic since 2005, *Nat.*
906 *Geosci.*, 9(7), doi:10.1038/ngeo2727, 2016.

907
908 Robson, J., Polo, I., Hodson, D. L. R., Stevens, D. P. and Shaffrey, L. C.: Decadal prediction of the North
909 Atlantic subpolar gyre in the HiGEM high-resolution climate model, *Clim. Dyn.*, 50(3), 921–937,
910 doi:10.1007/s00382-017-3649-2, 2018a.

911
912 Robson, J., Sutton, R. T., Archibald, A., Cooper, F., Christensen, M., Gray, L. J., Holliday, N. P.,
913 Macintosh, C., McMillan, M., Moat, B., Russo, M., Tilling, R., Carslaw, K., Desbroy eres, D., Embury, O., Feltham,
914 D. L., Grosvenor, D. P., Josey, S., King, B., Lewis, A., McCarthy, G. D., Merchant, C., New, A. L., O’Reilly, C. H.,
915 Osprey, S. M., Read, K., Scaife, A., Shepherd, A., Sinha, B., Smeed, D., Smith, D., Ridout, A., Woollings, T. and

916 Yang, M.: Recent multivariate changes in the North Atlantic climate system, with a focus on 2005–2016, *Int. J.*
917 *Climatol.*, 38(14), 5050–5076, doi:10.1002/joc.5815, 2018b.

918

919 Roussenov, V. M., Williams, R. G., Hughes, C. W. and Bingham, R. J.: Boundary wave communication of
920 bottom pressure and overturning changes for the North Atlantic, *J. Geophys. Res. Oceans*, 113(C8),
921 doi:10.1029/2007JC004501, 2008.

922

923 Schlesinger, M. E. and Ramankutty, N.: An oscillation in the global climate system of period 65-70 years,
924 *Nature*, 367(6465), 723–726, 1994.

925

926 Sgubin, G., Swingedouw, D., Drijfhout, S., Mary, Y. and Bennabi, A.: Abrupt cooling over the North
927 Atlantic in modern climate models, *Nat. Commun.*, 8 [online] Available from:
928 <http://dx.doi.org/10.1038/ncomms14375>, 2017.

929

930 Shaffrey, L., Stevens, I., Norton, W. A., Roberts, M. J., Vidale, P. L., Harle, J. D., Jrrar, A., Stevens, D. P.,
931 Woodage, M. J., Demory, M. E., Donners, J., Clark, D. B., Clayton, A., Cole, J. W., Wilson, S. S., Connolley, W. M.,
932 Davi, T. M. and Martin, G. M.: U.K. HiGEM: The New U.K. High-Resolution Global Environment Model—Model
933 Description and Basic Evaluation, *J. Clim.*, 22(8), 1861–1896, doi:10.1175/2008JCLI2508.1, 2009.

934

935 Sinha, B., Smeed, D. A., McCarthy, G., Moat, B. I., Josey, S. A., Hirschi, J. J.-M., Frajka-Williams, E.,
936 Blaker, A. T., Rayner, D. and Madec, G.: The accuracy of estimates of the overturning circulation from basin-wide
937 mooring arrays, *Prog. Oceanogr.*, 160, 101–123, doi:10.1016/j.pocean.2017.12.001, 2018.

938

939 Smeed, D. A., Josey, S. A., Beaulieu, C., Johns, W. E., Moat, B. I., Frajka-Williams, E., Rayner, D.,
940 Meinen, C. S., Baringer, M. O., Bryden, H. L. and McCarthy, G. D.: The North Atlantic Ocean Is in a State of
941 Reduced Overturning, *Geophys. Res. Lett.*, 45(3), 1527–1533, doi:10.1002/2017GL076350, 2018.

942

943 Smith, D. M. and Murphy, J. M.: An objective ocean temperature and salinity analysis using covariances
944 from a global climate model, *J. Geophys. Res. Oceans*, 112(C2), doi:10.1029/2005JC003172, 2007.

945

946 Sutton, R. T. and Hodson, D. L. R.: Atlantic Ocean forcing of North American and European summer
947 climate., *Science*, 309(2005), 115–118, doi:10.1126/science.1109496, 2005.

948

949 Sutton, R. T., McCarthy, G. D., Robson, J., Sinha, B., Archibald, A. T. and Gray, L. J.: Atlantic
950 Multidecadal Variability and the U.K. ACSIS Program, *Bull. Am. Meteorol. Soc.*, 99(2), 415–425,
951 doi:10.1175/BAMS-D-16-0266.1, 2018.

952

953 Tandon, N. F., and Kushner, P. J.: Does External Forcing Interfere with the AMOC's Influence on North
954 Atlantic Sea Surface Temperature?, *Journal of Climate*, 28, 6309-6323. 2015.

955

956 Taylor, K. E., Stouffer, R. J. and Meehl, G. A.: An Overview of CMIP5 and the Experiment Design, *Bull.*
957 *Am. Meteorol. Soc.*, 93(4), 485–498, doi:10.1175/BAMS-D-11-00094.1, 2012.

958

959 Thornalley, D. J. R., Oppo, D. W., Ortega, P., Robson, J. I., Brierley, C. M., Davis, R., Hall, I. R.,
960 Moffa-Sanchez, P., Rose, N. L., Spooner, P. T., Yashayaev, I. and Keigwin, L. D.: Anomalous weak Labrador Sea
961 convection and Atlantic overturning during the past 150 years, *Nature*, 556(7700), doi:10.1038/s41586-018-0007-4,
962 2018.

963

964 Storch, H., and Zwiers, F.: *Statistical Analysis in Climate Research*. Cambridge: Cambridge University
965 Press. doi:10.1017/CBO9780511612336, 1999.

966

967 Weijer, W., Cheng, W., Garuba, O. A., Hu, A. and Nadiga, B. T.: CMIP6 Models Predict Significant 21st
968 Century Decline of the Atlantic Meridional Overturning Circulation, *Geophys. Res. Lett.*, 47(12), e2019GL086075,
969 doi:10.1029/2019GL086075, 2020.

970
971 Woollings, T., Gregory, J., Pinto, J. G., Reyers, M. and Brayshaw, D.: Response of the North Atlantic storm
972 track to climate change shaped by ocean–atmosphere coupling, *Nat. Geosci.*, 5(5), 313–317, doi:10.1038/ngeo1438,
973 2012.
974
975 Xu, X., Chassignet, E. P. and Wang, F.: On the variability of the Atlantic meridional overturning circulation
976 transports in coupled CMIP5 simulations, *Clim. Dyn.*, 52(11), 6511–6531, doi:10.1007/s00382-018-4529-0, 2019.
977
978 Yan, X., Zhang, R. and Knutson, T. R.: Underestimated AMOC Variability and Implications for AMV and
979 Predictability in CMIP Models, *Geophys. Res. Lett.*, 45(9), 4319–4328, doi:10.1029/2018GL077378, 2018.
980
981 Yashayaev, I. and Loder, J. W.: Recurrent replenishment of Labrador Sea Water and associated
982 decadal-scale variability, *J. Geophys. Res. Oceans*, 121, 8095–8114, doi:10.1002/2016JC012046, 2016.
983
984 Yeager, S.: Topographic Coupling of the Atlantic Overturning and Gyre Circulations, *J. Phys. Oceanogr.*,
985 45(5), 1258–1284, doi:10.1175/JPO-D-14-0100.1, 2015.
986
987 Yeager, S. and Danabasoglu, G.: The Origins of Late-Twentieth-Century Variations in the Large-Scale
988 North Atlantic Circulation, *J. Clim.*, 27(9), 3222–3247, doi:10.1175/JCLI-D-13-00125.1, 2014.
989
990 Yeager, S. G. and Robson, J. I.: Recent Progress in Understanding and Predicting Atlantic Decadal Climate
991 Variability, *Curr. Clim. Change Rep.*, 3(2), 112–127, doi:10.1007/s40641-017-0064-z, 2017.
992
993 Zhang, L. and Wang, C.: Multidecadal North Atlantic sea surface temperature and Atlantic meridional
994 overturning circulation variability in CMIP5 historical simulations, *J. Geophys. Res. Oceans*, 118(10), 5772–5791,
995 doi:10.1002/jgrc.20390, 2013.
996
997 Zhang, R.: Coherent surface-subsurface fingerprint of the Atlantic meridional overturning circulation,
998 *Geophys. Res. Lett.*, 35, 1–6, doi:10.1029/2008GL035463, 2008.
999
1000 Zhang, R. and Delworth, T. L.: Impact of Atlantic multidecadal oscillations on India/Sahel rainfall and
1001 Atlantic hurricanes, *Geophys. Res. Lett.*, 33(17), doi:10.1029/2006GL026267, 2006.
1002
1003 Zhang, R., Delworth, T. L., Rosati, A., Anderson, W. G., Dixon, K. W., Lee, H. C. and Zeng, F.: Sensitivity
1004 of the North Atlantic Ocean Circulation to an abrupt change in the Nordic Sea overflow in a high resolution global
1005 coupled climate model, *J. Geophys. Res. Oceans*, 116, 1–14, doi:10.1029/2011JC007240, 2011.
1006
1007 Zhao, J. and Johns, W.: Wind-forced interannual variability of the Atlantic Meridional Overturning
1008 Circulation at 26.5 N, *J. Geophys. Res. Oceans*, 2403–2419, doi:10.1002/2013JC009407.Received, 2014.
1009
1010 Zou, S., Lozier, M. S. and Xu, X.: Latitudinal Structure of the Meridional Overturning Circulation
1011 Variability on Interannual to Decadal Time Scales in the North Atlantic Ocean, *J. Clim.*, 33(9), 3845–3862,
1012 doi:10.1175/JCLI-D-19-0215.1, 2020.
1013